Fluid Simulation on Compressible Flow Maps

DUOWEN CHEN*, Georgia Institute of Technology, USA
ZHIQI LI*, Georgia Institute of Technology, USA
TAIYUAN ZHANG, Dartmouth College, USA
JINJIN HE, Dartmouth College, USA
JUNWEI ZHOU, University of Michigan, , USA
BART G. VAN BLOEMEN WAANDERS, Sandia National Laboratories, USA
BO ZHU, Georgia Institute of Technology, USA

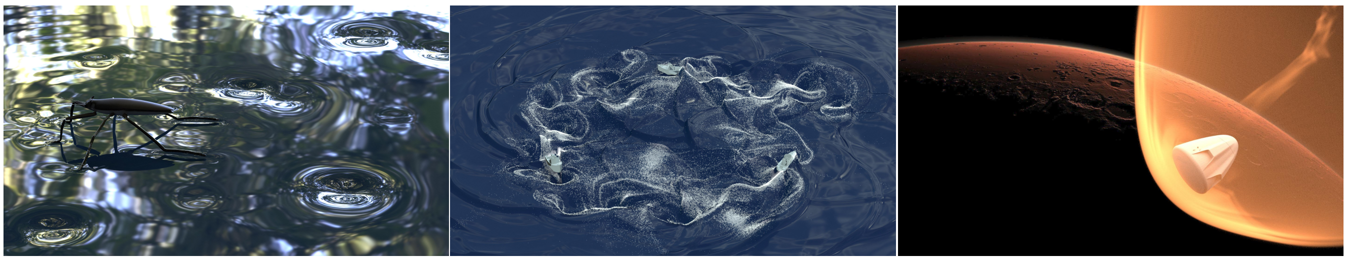

Fig. 1. We present diverse phenomena simulated using our compressible flow map method. From small-scale water striders swimming on the surface of a pond, to large-scale ships on vast oceans, and a Dragon capsule landing on Mars, our simulator captures both compressible and weakly compressible dynamics spanning various scales of applications with a single unified framework.

This paper presents a unified compressible flow map framework designed to accommodate diverse compressible flow systems, including high-Mach-number flows (e.g., shock waves and supersonic aircraft), weakly compressible systems (e.g., smoke plumes and ink diffusion), and incompressible systems evolving through compressible acoustic quantities (e.g., free-surface shallow water). At the core of our approach is a theoretical foundation for compressible flow maps based on Lagrangian path integrals, a novel advection scheme for the conservative transport of density and energy, and a unified numerical framework for solving compressible flows with varying pressure treatments. We validate our method across three representative compressible flow systems, characterized by varying fluid morphologies, governing equations, and compressibility levels, demonstrating its ability to preserve and evolve spatiotemporal features such as vortical structures and wave interactions governed by different flow physics. Our results highlight a wide range of novel phenomena, from ink torus breakup to delta wing tail vortices and vortex shedding on free surfaces, significantly expanding the range of fluid systems that flow-map methods can handle.

CCS Concepts: • **Computing methodologies** → **Physical simulation**.

*Joint first authors

Authors' Contact Information: Duowen Chen, dchen322@gatech.edu, Georgia Institute of Technology, USA; Zhiqi Li, zli3167@gatech.edu, Georgia Institute of Technology, USA; Taiyuan Zhang, taiyuan.zhang.gr@dartmouth.edu, Dartmouth College, USA; Jinjin He, jinjin.he.gr@dartmouth.edu, Dartmouth College, USA; Junwei Zhou, zjw330501@gmail.com, University of Michigan,, USA; Bart G. van Bloemen Waanders, bartv@sandia.gov, Sandia National Laboratories, USA; Bo Zhu, bo.zhu@gatech.edu, Georgia Institute of Technology, USA.

ACM 1557-7368/2025/8-ART
https://doi.org/10.1145/3731192

Additional Key Words and Phrases: Compressible Flow, Flow Maps Method, Impulse Gauge Fluid, Vortex Dynamics, Shock Waves, Shallow Water

ACM Reference Format:
Duowen Chen, Zhiqi Li, Taiyuan Zhang, Jinjin He, Junwei Zhou, Bart G. van Bloemen Waanders, and Bo Zhu. 2025. Fluid Simulation on Compressible Flow Maps. *ACM Trans. Graph.* 44, 4 (August 2025), 17 pages. https://doi.org/10.1145/3731192

1 Introduction

Flow-map methods have gained increasing attention in both computer graphics and computational physics for their geometric intuition in transporting fluid elements and their demonstrated ability to reduce numerical dissipation during flow convection (e.g., see [Deng et al. 2023; Nabizadeh et al. 2022; Yin et al. 2021, 2023; Zhou et al. 2024]). When combined with a Lagrangian gauge variable such as impulse or vorticity, flow-map methods have been successfully applied to simulate a broad range of flow systems, including vortex streets [Wang et al. 2024], particle-laden flows [Li et al. 2024b], free-surface splashes [Li et al. 2024a], and solid-fluid couplings [Chen et al. 2024], to name just a few. These methods have consistently showcased impressive capabilities in accurately addressing the difference between vortical structures and physical elements in a variety of flow settings.

However, despite the incorporation of various physical elements into the flow-map framework, previous studies have exclusively focused on incompressible fluids. Two reasons underlie this limitation: (1) For the *advection* step, the flow-map schemes available for point, line, and surface elements are only applicable in incompressible settings, as their derivations assume the velocity field is divergence-free (see [Wu et al. 2007]); (2) For the *projection* step, typical flow-map solvers rely on a Poisson system to project the gauge variable (e.g., impulse) back to velocity at each timestep, which only functions in incompressible settings by projecting out the curl-free component based on Helmholtz decomposition.

Compressible flows, by contrast, have not yet been integrated into the blueprint of flow-map methods, thereby excluding a wide range of highly compressible or weakly compressible fluid systems that could potentially benefit from the flow map's exceptional vorticity evolution capabilities. These flow phenomena include not only the traditionally recognized *high-Mach-number compressible gases* (such as shock waves, rocket launches, or supersonic aircraft breaking sound barriers) but also many *incompressible fluid systems* commonly encountered in other practical problems, where fluid velocity evolves in a compressible manner by advancing a certain "acoustic" quantity related to pressure (e.g., the fluid height in shallow water or the film thickness in soap bubbles). Furthermore, compressible flow systems encompass an important category of *weakly compressible fluids*, whose flow behavior closely resembles that of incompressible fluids when the compression ratio is visually negligible. These fluids have been widely simulated in graphics applications to mimic their incompressible counterparts. A wide range of classical simulation algorithms, such as SPH [Brookshaw 1985], MPM [Jiang et al. 2016], and LBM [Chen and Doolen 1998], all fall into this category.

This paper addresses the challenges of facilitating compressible fluid simulation using flow-map techniques. We have developed a unified and versatile compressible flow map framework to accommodate various types of compressible systems, as surveyed above, ranging from supersonic sound barriers and free-surface wave-vortex interactions to weakly compressible fluid phenomena such as smoke plumes and ink diffusion. We tackle the problem from both theoretical and algorithmic perspectives. On the theoretical side, we propose a unified compressible flow map model based on Lagrangian path integrals, with the formal incompressible flow map formula as a special case. Building on this novel compressible flow-map model, we further develop a unified simulation algorithm to conservatively evolve quantities such as density and energy over long ranges on a non-divergence-free velocity field. The evolution of these quantities naturally preserves and evolves flow features (such as complex vortical structures on a free surface), which have been infeasible for previous compressible flow solvers. This enables a broad range of new flow phenomena to be simulated using our flow-map techniques, thereby producing physically based vortical structures and their interactions with compressible waves that have not been captured previously. These phenomena range from ink torus breakup to delta wing tail vortices, from shocks generated by the Dragon return capsule to water striders walking on water surfaces, and from ships navigating vast oceans to vortices on small-scale surfaces, demonstrating the capability of flow-map methods outside their original incompressible domain.

We summarize our contributions as follows:

(1) We derive a compressible flow map model capable of characterizing both compressible and incompressible flow systems.
(2) We develop a novel advection scheme based on Lagrangian path integrals to conservatively transport physical quantities in compressible flow fields.
(3) We propose a unified numerical framework to solve compressible flow problems with various pressure treatments.
(4) We demonstrate the applications of our compressible flow-map solver in addressing shallow water, shock waves, and weakly compressible fluids, showcasing a wide range of phenomena across different substances, Mach numbers, and vortex-wave interactions.

2 Related Work

Shallow Water. To reduce the cost of simulating large fluid surfaces using the full incompressible Navier-Stokes equation, shallow water approximation [De St Venant 1871] was proposed seeking improvement on previous Airy wave theory simulation [Airy 1845] which assumes the fluid is irrotational and inviscid. Subsequent developments enabled the creation of splashing effects [Chentanez et al. 2015; O'brien and Hodgins 1995] and the coupling of solids and fluids [Chen et al. 1997] within the Shallow Water framework. The transition of Shallow Water simulations to GPU processing was pioneered by Hagen et al. [2005]. Further research explored solving Shallow Water on water surface meshes [Wang et al. 2007], utilizing Smoothed Particle Hydrodynamics (SPH) [Lee and Han 2010; Solenthaler et al. 2011], and integrating non-reflective boundary conditions [Chentanez and Müller 2010]. Recent advancements have enhanced the vorticity wake effects [Pan et al. 2012], enriching surface detail through synthesized approaches. Additionally, Jeschke and Wojtan [2023] expanded the scope of Shallow Water by enabling the simulation of dispersive waves. Despite efforts to enhance the convection term in SWE for vortex preservation, as attempted in [Pan et al. 2012], effectively inducing and maintaining surface vortical structures using SWE remains challenging.

Shock Wave. In graphics, early developments in shock wave simulations relied on explicit discretizations of the compressible Euler equations [Yngve et al. 2000]. Sewall et al. [2009] introduced a finite volume Riemann solver to improve performance. A comprehensive review preceding the suggestion to solve the compressible Euler's Equations implicitly was presented in [Fedkiw et al. 2003]. However, explicit approaches suffer from strict CFL constraints, limiting scalability to large domains or high resolutions. Kwatra et al. [2010, 2009] addressed this with the Mach Poisson solver—an incompressible-style Poisson formulation that relaxes CFL restrictions by solving a modified pressure equation. Combined with ENO/WENO [Liu et al. 1994; Shu and Osher 1988] schemes and TVD-RK advection, this approach enables stable Euler equation solutions on a grid. Grétarsson et al. [2011] improved solution robustness for shock-solid interactions, and Grétarsson and Fedkiw [2013] ensured mass conservation. Recent extensions cover subgrid-scale modeling [Hyde and Fedkiw 2019] and MPM coupling for soft bodies [Cao et al. 2022].

Weakly Compressible Flow. Mainstream methods for simulating weakly compressible flows are primarily categorized into three types: Smoothed Particle Hydrodynamics (SPH) [Brookshaw 1985], Material Point Method (MPM) [Jiang et al. 2016], and Lattice Boltzmann Method (LBM) [Chen and Doolen 1998]. These methods have been widely applied across various scenarios, including simulating smoke [Gao et al. 2009; Stam and Fiume 1995; Zhu et al. 2010], free surface fluids [Becker and Teschner 2007], enabling two-way coupling [Hu et al. 2018; Lyu et al. 2021], and low Mach aircraft [Lyu et al. 2023] motions within wind tunnel environments. However, methods like SPH struggle with vorticity preservation, and to the best of our knowledge, there have been no compressible solvers in the graphics community proposed for either MPM or LBM that adequately address the simulation of shock waves.

Flow Map Methods. Flow maps were first introduced by Wiggert and Wylie [1976]. This technique, which reduces diffusion error in semi-Lagrangian advection, inspired numerous adaptations in the graphics community for fluid simulation [Hachisuka 2005; Qu et al. 2019; Sato et al. 2018, 2017; Tessendorf 2015]. Later, Nabizadeh et al. [2022] utilized flow map for advection in the gauge variable framework. Building on these foundations, the Neural Flow Map (NFM) [Deng et al. 2023] introduced neural networks to improve the accuracy of flow maps. Hybrid approaches such as Particle Flow Map (PFM) [Zhou et al. 2024], Impulse PIC (IPIC) [Sancho et al. 2024] and CO-FLIP [Nabizadeh et al. 2024] have merged particle techniques with flow maps. Li et al. [2024a] extended flow map methods to simulation with pure Lagrangian representations. Most recently, flow maps have also been adapted to vortex method [Wang et al. 2024] and been used to simulate various phenomena including particle-laden flow [Li et al. 2024b], two-phase flow [Sun et al. 2024] and solid-fluid coupling [Chen et al. 2024]. Our method aims to unify previous research on incompressible simulation domains within a unified compressible and weakly compressible simulation framework without harming visual quality.

3 Mathematical Background

Consider a fluid that flows from the initial domain $\mathbb{U}_s$ at time s, governed by a velocity field $\mathbf{u}(\mathbf{x}, t), \mathbf{x} \in \mathbb{U}_t, t \geq s$, where $\mathbb{U}_t$ is the domain of the fluid at time t. For any two times $t_1, t_2 \geq s$, define the forward flow map $\mathbf{\Phi}_{t_1 \to t_2} : \mathbb{U}_{t_1} \to \mathbb{U}_{t_2}$ and the backward flow map $\mathbf{\Psi}_{t_2 \to t_1} : \mathbb{U}_{t_2} \to \mathbb{U}_{t_1}$, such that for any fluid particle p moving according to the velocity field $\mathbf{u}(\mathbf{x}, t)$, the position $\mathbf{x}_p(t_1)$ of p at time t_1 and the position $\mathbf{x}_p(t_1)$ at time t_2 satisfy the relations $\mathbf{\Phi}_{t_1 \to t_2}(\mathbf{x}_p(t_1)) = \mathbf{x}_p(t_2)$ and $\mathbf{\Psi}_{t_2 \to t_1}(\mathbf{x}_p(t_2)) = \mathbf{x}_p(t_1)$. The Jacobians of the forward and backward flow maps are defined as $\mathcal{F}_{t_1 \to t_2}(\mathbf{x}) = \frac{\partial \mathbf{\Phi}_{t_1 \to t_2}(\mathbf{x})}{\partial \mathbf{x}}, \mathbf{x} \in \mathbb{U}_{t_1}$ and $\mathcal{T}_{t_2 \to t_1}(\mathbf{x}) = \frac{\partial \mathbf{\Psi}_{t_2 \to t_1}(\mathbf{x})}{\partial \mathbf{x}}, \mathbf{x} \in \mathbb{U}_{t_2}$, respectively. The flow maps $\mathbf{\Phi}_{s \to t}$, $\mathbf{\Psi}_{t \to s}$ and their Jacobians, are evolved as:

$$\begin{cases} \frac{\partial \mathbf{\Phi}_{s \to t}(\mathbf{x})}{\partial t} = \mathbf{u}(\mathbf{\Phi}_{s \to t}(\mathbf{x}), t), & \mathbf{\Phi}_{s \to s}(\mathbf{x}) = \mathbf{x} \\ \frac{\partial \mathcal{F}_{s \to t}(\mathbf{x})}{\partial t} = \nabla \mathbf{u}(\mathbf{\Phi}_{s \to t}(\mathbf{x}), t)\mathcal{F}_{s \to t}(\mathbf{x}), & \mathcal{F}_{s \to s}(\mathbf{x}) = \mathbf{I} \end{cases} \tag{1}$$

$$\begin{cases} \frac{D\mathbf{\Psi}_{t \to s}(\mathbf{x})}{Dt} = 0, & \mathbf{\Psi}_{s \to s}(\mathbf{x}) = \mathbf{x} \\ \frac{D\mathcal{T}_{t \to s}(\mathbf{x})}{Dt} = -\mathcal{T}_{t \to s}(\mathbf{x})\nabla \mathbf{u}(\mathbf{x}, t), & \mathcal{T}_{s \to s}(\mathbf{x}) = \mathbf{I} \end{cases} \tag{2}$$

Equations 1 and 2 can be solved using a Lagrangian or Eulerian perspective, which we briefly review as follows.

Lagrangian flow maps. A Lagrangian flow map uses particles $p \in \mathcal{P}$ to sample the fluid domain. Each particle $\mathbf{x}_p(t)$ at time t carries corresponding Jacobians $\mathcal{F}_p(t) = \mathcal{F}_{s \to t}(\mathbf{x}_p(s))$ and $\mathcal{T}_p(t) = \mathcal{T}_{t \to s}(\mathbf{x}_p(t))$, initiated from $\mathbf{x}_{p,0}$. The particle position $x_p(t)$ and the Jacobians $\mathcal{F}_p(t)$ and $\mathcal{T}_p(t)$ are evolved as:

$$\begin{aligned} &\frac{d\mathbf{x}_p(t)}{dt} = \mathbf{u}(\mathbf{x}_p(t), t), && \mathbf{x}_p(s) = \mathbf{x}_{p,0} \\ &\begin{cases} \frac{d\mathcal{F}_p(t)}{dt} &= \nabla \mathbf{u}(\mathbf{x}_p(t), t)\mathcal{F}_p(t) \\ \frac{d\mathcal{T}_p(t)}{dt} &= -\mathcal{T}_p(t)\nabla \mathbf{u}(\mathbf{x}_p(t), t) \end{cases}, && \mathcal{F}_p(s) = \mathcal{T}_p(s) = \mathbf{I} \end{aligned} \tag{3}$$

where $\mathbf{I}$ is the identity matrix.

Eulerian flow maps. An Eulerian flow map discretizes the fluid domain on a grid. It evolves $\mathbf{\Phi}_{s \to t}(\mathbf{x})$ and $\mathcal{F}_{s \to t}(\mathbf{x})$ on the grid according to Equation 1. At each time step r, it starts from the current time step r and traces backwards with a velocity buffer to evolve $\mathbf{\Psi}_{r \to t}(\mathbf{x})$ and $\mathcal{T}_{r \to t}(\mathbf{x})$, yielding $\mathbf{\Psi}_{r \to s}(\mathbf{x})$ and $\mathcal{T}_{r \to s}(\mathbf{x})$:

$$\begin{cases} \frac{\partial \mathbf{\Psi}_{r \to t}(\mathbf{x})}{\partial t} = \mathbf{u}(\mathbf{\Psi}_{r \to t}(\mathbf{x}), t), & \Phi_{r \to r}(\mathbf{x}) = \mathbf{x} \\ \frac{\partial \mathcal{T}_{r \to t}(\mathbf{x})}{\partial t} = \nabla \mathbf{u}(\mathbf{\Psi}_{r \to t}(\mathbf{x}), t)\mathcal{T}_{r \to t}(\mathbf{x}), & \mathcal{T}_{r \to r}(\mathbf{x}) = \mathbf{I} \end{cases} \tag{4}$$

Incompressible flow on flow maps. Let $\mathbf{u}^M_{s \to t}$ be the mapped velocity using flow map Jacobian $\mathbf{u}^M_{s \to t}(\mathbf{x}) = \mathcal{T}_{t \to s}(\mathbf{x})^\top \mathbf{u}(\mathbf{\Psi}_{t \to s}(\mathbf{x}), s)$. For an incompressible fluid without external forces, the mapped velocity $\mathbf{u}^M_{s \to t}$ also serves as the impulse variable $\mathbf{m}_t$, i.e., $\mathbf{m}_t(\mathbf{x}) = \mathbf{u}^M_{s \to t}(\mathbf{x})$ [Cortez 1996]. Since the impulse $\mathbf{m}_t$ is a gauge transformation of the velocity $\mathbf{u}_t$, there exists a scalar field Λ_t such that $\mathbf{m}_t = \mathbf{u}_t + \nabla \Lambda_t$, where Λ_t satisfies the evolution equation $\frac{D\Lambda_t}{Dt} = -\frac{1}{\rho}\nabla p + \frac{1}{2}\nabla |\mathbf{u}|^2$[Cortez 1996; Nabizadeh et al. 2022]. Using the impulse variable, the fluid velocity can be expressed as:

$$\begin{aligned} &\mathbf{m}_t(\mathbf{x}) = \mathcal{T}^\top_{t \to s}(\mathbf{x})\mathbf{u}_s(\mathbf{\Psi}_{\mathbf{t} \to \mathbf{s}}(\mathbf{x})), \\ &\mathbf{u}_t(\mathbf{x}) = \mathbf{m}_t(\mathbf{x}) - \nabla \Lambda_t(\mathbf{x}), \qquad \Delta \Lambda_t = \nabla \cdot \mathbf{m}_t. \end{aligned} \tag{5}$$

Here, Λ_t can be obtained from the Poisson equation in the second line, rather than solving its evolution equation, since $\mathbf{m}_t = \mathbf{u}_t + \nabla \Lambda_t$ forms the Helmholtz decomposition of $\mathbf{m}_t$.

4 Compressible Flow Map

4.1 Physical Equations

4.1.1 Compressible flow. We consider the following compressible fluid system:

$$\begin{aligned} \frac{D\mathbf{u}}{Dt} &= -\frac{1}{\rho}\nabla p + \mathbf{f}, \\ \frac{D\rho}{Dt} &= -(\nabla \cdot \mathbf{u})\rho. \end{aligned} \tag{6}$$

This system is not closed for unknown pressure p. Due to the diverse sources of pressure calculation under compressible flow conditions, the system can be closed using various methods of pressure determination, such as from the height field in Shallow Water, from the equation of state (EOS) in shock waves, or from solving a complex variable Poisson equation namely Mach Poisson [Kwatra et al. 2009].

4.1.2 Gauge transform. In incompressible fluids, the impulse $\mathbf{m}_t = \mathbf{u}_t + \nabla \Lambda_t$ naturally forms a Helmholtz decomposition for divergence-free velocity field u and constant-coefficient pressure term ∇p. In compressible fluids, however, the time-dependent density in $\frac{1}{\rho}\nabla p$ and the lack of divergence-free velocity fields make the problem more complex. Therefore, to apply the flow map framework to compressible fluids and leverage its notable advantage of strong vortex preservation, the first challenge is to define a suitable impulse gauge transformation and to formulate a method for computing the impulse in compressible flows.

Analogous to the impulse formulation in incompressible fluids, Shivamoggi [2010] and Pareja [2007] define the impulse gauge transformation for compressible fluids as

$$\mathbf{m}_t = \mathbf{u}_t + \frac{1}{\rho_t}\nabla\tilde{\Lambda}_t \tag{7}$$

where the density ρ_t is time-dependent and spatially varying. However, unlike the incompressible case described in (5), they did not derive a general form for $\mathbf{m}_t$ due to the added complexity introduced by the dependence on ρ_t. They only showed that under the barotropic condition with time-invariant density $\frac{\partial\rho}{\partial t} = 0$, the relation $\mathbf{m}_t(\mathbf{x}) = \mathcal{T}^\top_{t\to s}(\mathbf{x})\mathbf{u}_s(\Psi_{t\to s}(\mathbf{x}))$ still holds for computing $\mathbf{m}_t(\mathbf{x})$. **We extend this result by resolving the computation of $\mathbf{m}_t(\mathbf{x})$ under more general barotropic condition without the time-invariant density constraint**, enabling the impulse to be properly defined and computed in a broader range of applications—including all scenarios commonly encountered in computer graphics. Under the barotropic condition, the impulse is computed as follows (see Appendix A for the proof):

$$\begin{aligned}
&\mathbf{m}_t(\mathbf{x}) = \frac{\mathcal{T}^\top_{t\to s}(\mathbf{x})}{|\mathcal{T}_{t\to s}(\mathbf{x})|}\mathbf{u}_s(\Psi_{t\to s}(\mathbf{x})) + \frac{\mathcal{T}^\top_{t\to s}(\mathbf{x})}{|\mathcal{T}_{t\to s}(\mathbf{x})|}\mathcal{E}_{s\to t}(\Psi_{t\to s}(\mathbf{x})),\\
&\mathcal{E}_{s\to t}(\mathbf{x}) = \int_s^t \frac{\mathcal{F}^\top_{s\to\tau}(\mathbf{x})}{|\mathcal{F}_{s\to\tau}(\mathbf{x})|}\left(-\frac{\nabla\rho}{2\rho}|\mathbf{u}|^2 - (\nabla\cdot\mathbf{u})\mathbf{u} + \mathbf{f}\right)(\Phi_{s\to\tau}(\mathbf{x}), \tau)d\tau,\\
&\mathbf{u}_t(\mathbf{x}) = \mathbf{m}_t(\mathbf{x}) - \frac{1}{\rho_t}\nabla\tilde{\Lambda}_t(\mathbf{x}),
\end{aligned} \tag{8}$$

where $\tilde{\Lambda}_t$ satisfies the advection equation $\frac{D\tilde{\Lambda}_t}{Dt} = p_t - \frac{1}{2}\rho_t|\mathbf{u}_t|^2$. Here, $|\cdot|$ represents matrix determinant for flow map Jacobians and vector norms for vector quantities. We show that $\tilde{\Lambda}_t$ can be expressed in integral form as:

$$\tilde{\Lambda}_t(\mathbf{x}) = \int_s^t \left(p - \frac{1}{2}\rho|\mathbf{u}|^2\right)(\Phi_{s\to\tau}\circ\Psi_{t\to s}(\mathbf{x}), \tau)d\tau. \tag{9}$$

As shown in the equations above, unlike the incompressible case in Equation 5, we cannot trivially write down a simple mapping form for $\mathbf{m}_t$ due to its additional dependence on ρ_t. Instead, the mapping of $\mathbf{m}_t$ involves several quantities, such as the Jacobian determinant, velocity divergence, and density gradient, which are only present in the case of compressible flow. In this compressible case, the long-term mapped velocity is given by $\mathbf{u}^M_{s\to t}(\mathbf{x}) = \frac{\mathcal{T}^\top_{t\to s}(\mathbf{x})}{|\mathcal{T}_{t\to s}(\mathbf{x})|}\mathbf{u}_s(\Psi_{t\to s}(\mathbf{x}))$. Equation 5 for incompressible fluids is a special case of this equation with $\Lambda_t = \frac{1}{\rho_t}\tilde{\Lambda}_t$ when ρ_t is constant, $\nabla\cdot\mathbf{u} = 0$ and $|\mathcal{T}_{t\to s}| = |\mathcal{F}_{s\to t}| = 1$ under the incompressible condition.

4.1.3 Notes on projection. Notably, for compressible fluids, the computation from $\mathbf{m}$ to $\mathbf{u}$ differs from the incompressible case, where Λ_t is obtained via a projection step by solving a Poisson equation. In a compressible system, $\mathbf{m}_t = \mathbf{u}_t + \frac{1}{\rho_t}\nabla\tilde{\Lambda}_t$ does not represent the Helmholtz decomposition of $\mathbf{m}_t$, making it impractical to derive a projection step for the long-term integration of Λ from the pressure p. Therefore, $\tilde{\Lambda}_t$ in Equation 8 should be computed by integrating Equation 9, and $\mathcal{E}_{s\to t}$ is obtained using the same approach.

4.2 Unified Flow-Map Model

Because both $\tilde{\Lambda}_t$ and $\mathcal{E}_{s\to t}$ in Equation 8 require integration, we aim to simplify the computation by merging these two integral forms, namely merging $\frac{\mathcal{T}^\top_{t\to s}}{|\mathcal{T}_{t\to s}|}\mathcal{E}_{s\to t}(\Psi_{t\to s}(\mathbf{x}))$ and $-\frac{1}{\rho_t}\nabla\tilde{\Lambda}_t(\mathbf{x})$. By substituting the expression of $\mathbf{m}_t(\mathbf{x})$ from Equation 8 into the expression for $\mathbf{u}_t(\mathbf{x})$, and transforming $\tilde{\Lambda}_t$ to incorporate both $\tilde{\Lambda}_t$ and $\mathcal{E}_{s\to t}$, we obtain the flow map-based formula for computing $\mathbf{u}_t(\mathbf{x})$ (see Appendix B for details):

$$\boxed{\mathbf{u}_t(\mathbf{x}) = \underbrace{\frac{\mathcal{T}^\top_{t\to s}(\mathbf{x})}{|\mathcal{T}_{t\to s}(\mathbf{x})|}\mathbf{u}_s(\Psi_{t\to s}(\mathbf{x}))}_{\text{mapping}} + \underbrace{\frac{\mathcal{T}^\top_{t\to s}(\mathbf{x})}{|\mathcal{T}_{t\to s}(\mathbf{x})|}\tilde{\mathcal{E}}_{s\to t}(\Psi_{t\to s}(\mathbf{x}))}_{\text{path integral}}} \tag{10}$$

where $\tilde{\mathcal{E}}_{s\to t}$ is defined as

$$\tilde{\mathcal{E}}_{s\to t}(\mathbf{x}) = \int_s^t \frac{\mathcal{F}^\top_{s\to\tau}(\mathbf{x})}{|\mathcal{F}_{s\to\tau}(\mathbf{x})|}\left(-\frac{1}{\rho}\nabla p + \frac{1}{2}\nabla|\mathbf{u}|^2 - (\nabla\cdot\mathbf{u})\mathbf{u} + \mathbf{f}\right)(\Phi_{s\to\tau}(\mathbf{x}), \tau)d\tau, \tag{11}$$

Considering the special case of an incompressible fluid where $|\mathcal{T}_{t\to s}| = |\mathcal{F}_{s\to\tau}| = 1$ and $\nabla\cdot\mathbf{u} = 0$, we have

$$\boxed{\mathbf{u}_t(\mathbf{x}) = \underbrace{\mathcal{T}^\top_{t\to s}(\mathbf{x})\mathbf{u}_s(\Psi_{t\to s}(\mathbf{x}))}_{\text{mapping}} + \underbrace{\mathcal{T}^\top_{t\to s}(\mathbf{x})\tilde{\mathcal{E}}_{s\to t}(\Psi_{t\to s}(\mathbf{x}))}_{\text{path integral}}} \tag{12}$$

with $\tilde{\mathcal{E}}_{s\to t}(\mathbf{x})$

$$\tilde{\mathcal{E}}_{s\to t}(\mathbf{x}) = \int_s^t \mathcal{F}^\top_{s\to\tau}(\mathbf{x})\left(-\frac{1}{\rho}\nabla p + \frac{1}{2}\nabla|\mathbf{u}|^2 + \mathbf{f}\right)(\Phi_{s\to\tau}(\mathbf{x}), \tau)d\tau \tag{13}$$

Surprisingly, Equation 10 and its incompressible counterpart, Equation 12, remain equivalent even in the compressible case (see Appendix C for proof). Moreover, equations 10 and 12 can be used interchangeably for calculating both compressible and incompressible flow maps, providing a unified flow-map model for both fluid types. Although Eq. 10, using mapping based on $\frac{\mathcal{F}^\top_{s\to\tau}(\mathbf{x})}{|\mathcal{F}_{s\to\tau}(\mathbf{x})|}$ and $\frac{\mathcal{T}^\top_{t\to s}(\mathbf{x})}{|\mathcal{T}_{t\to s}(\mathbf{x})|}$, seems to better reflect the nature of compressible flows, our experiments show that not only are Equation 12 and 10 mathematically equivalent, but their accuracy is also nearly indistinguishable (see the experiments in Sec. 9.1). Therefore, for the sake of lower computational cost and greater implementation simplicity, we will primarily focus on using Equation 12 to solve various compressible or weakly compressible flow systems in the subsequent sections. Equations 12 and 13 can also be derived directly using 1-form notation and Lie derivatives (see Appendix C for details). Here, we adopt a vector-based formulation to maintain consistency with the impulse literature [Pareja 2007; Shivamoggi 2010].

4.3 Physical Quantity Transport

With the compressible flow-map algorithm established, we now develop the physical quantity transport formula based on it.

4.3.1 Velocity Mapping. Velocity mapping is achieved using the flow map Jacobian which consists of the first part of Equation 12 similar to the usage under incompressible setting.

$$\mathbf{u}^M_{s\to t}(\mathbf{x}) = \mathcal{T}_{t\to s}(\mathbf{x})^\top\mathbf{u}(\Psi_{t\to s}(\mathbf{x}), s) \tag{14}$$

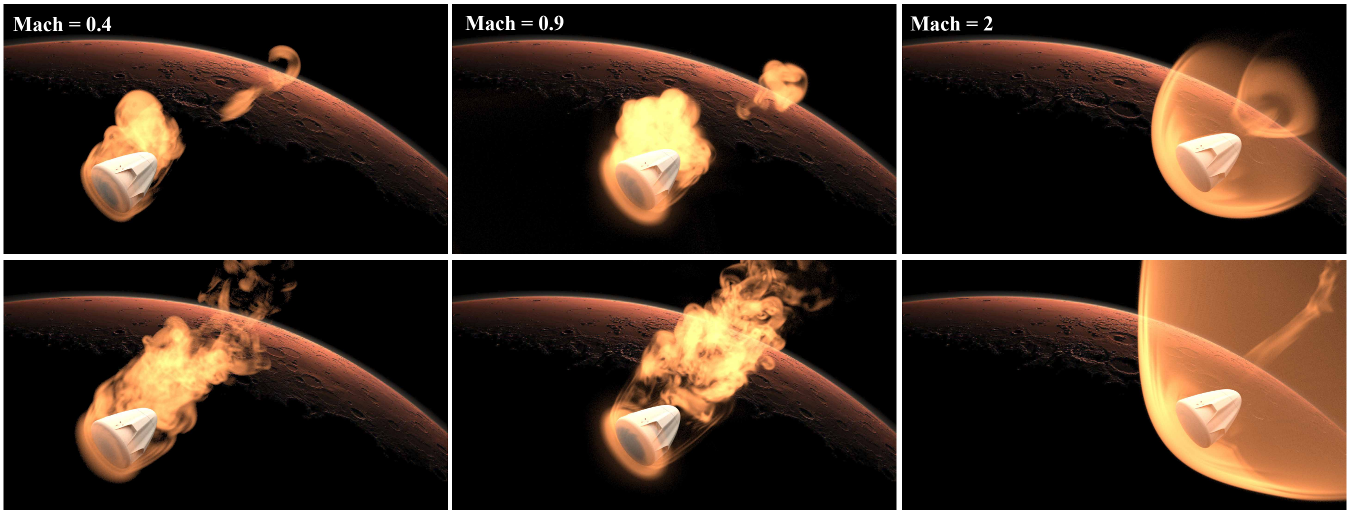

Fig. 2. We simulate a Dragon Capsule landing on Mars, matching results from [Spa 2015].

where $\mathbf{u}^M_{s\to t}(\mathbf{x})$ is the mapped velocity evaluated at time t and $\mathbf{u}(\mathbf{\Psi}_{t\to s}(\mathbf{x}), s)$ is the velocity at initial time s. $\mathcal{T}_{t\to s}(\mathbf{x})^\top$ denotes transpose of the backward flow map Jacobian.

4.3.2 Conservative Quantity Mapping. Unlike the incompressible setting where impulse and velocity are the primary quantities being mapped, in a compressible setting, a flow-map model also facilitates the transport of other quantities, such as density and energy, whose evolution can be summarized as:

$$\begin{cases} \frac{Dq}{Dt} = -\theta(\nabla\cdot\mathbf{u})q \\ q(\mathbf{x}, s) = q_s(\mathbf{x}), \quad \mathbf{x}\in\mathbb{U}_s, \end{cases} \tag{15}$$

where q represents a scalar field (e.g., density, energy, or height field) and θ is a constant. The long-range flow-map expression of the quantity transported in Equation 15 can be written as (see Appendix E for a proof):

$$q(\mathbf{x}, t) = |\mathcal{T}_{s\to t}(\mathbf{x})|^\theta q_s(\mathbf{\Psi}(\mathbf{x}, t)), \tag{16}$$

in which $|\mathcal{T}_{s\to t}(\mathbf{x})|$ denotes the determinant of flow map Jacobian $\mathcal{T}$ evaluated at time t and θ represents the constant used in conservative quantity advection where $\theta = 1$ for density or height field and $\theta = \gamma - 1$ for energy field. We refer readers to Sections 5.1 and 5.2.1 for different examples of q in different fluid systems.

4.4 Pressure Projection & Path Integral

We now describe our approach to solving the path integral in Equation 12 to recover the fluid velocity field. Unlike incompressible flows—where velocity is obtained by solving a Poisson equation for pressure and removing its gradient—compressible flows require distinct treatments depending on the pressure source. Specifically, velocity can be computed by evolving a height field (as in shallow water) or by solving a variable-coefficient Poisson system (as in shock simulations). We refer to these as **Acoustic Pressure** and **Poisson Pressure** systems, respectively. The procedures are outlined below:

4.4.1 Velocity Conversion: To accommodate these different cases for pressure projection, we propose a long-short flow map transformation scheme to calculate $\mathbf{u}_t(\mathbf{x})$ based on the long-range mapped velocity $\mathbf{u}^M_{s\to t}(\mathbf{x})$. In particular, we convert $\mathbf{u}^M_{s\to t}(\mathbf{x})$ to $\mathbf{u}^A_{t'\to t}(\mathbf{x})$ using a path integral maintained along the trajectory of each flow map

$$\begin{aligned}\mathbf{u}^A_{s\to t}(\mathbf{x}) = \mathbf{u}^M_{s\to t}(\mathbf{x}) + \\ \mathcal{T}^\top_{t\to s}(\mathbf{x})\tilde{\mathcal{E}}_{s\to t'}(\mathbf{\Psi}_{t\to s}(\mathbf{x})) + (\frac{1}{2}\nabla|\mathbf{u}_t|^2 + \mathbf{f}_t)(\mathbf{x})\Delta t\end{aligned} \tag{17}$$

where $\tilde{\mathcal{E}}_{s\to t'}(\mathbf{\Psi}_{t\to s}(\mathbf{x}))$ being the path integral.

4.4.2 Pressure Projection. After conversion, the pressure projection for $\mathbf{u}^A_{t'\to t}(\mathbf{x})$ can be solved by taking any of the conventional projection methods for compressible flow and updated as

$$\mathbf{u}_t(\mathbf{x}) = \mathbf{u}^A_{t'\to t}(\mathbf{x}) - \mathbf{f}_p\Delta t \tag{18}$$

4.4.3 Path Integral. With a calculated pressure, the path integral can now be evaluated using

$$\begin{aligned}\tilde{\mathcal{E}}_{s\to t}(\mathbf{x}) = \tilde{\mathcal{E}}_{s\to t'}(\mathbf{x}) + \\ \mathcal{F}^\top_{t\to s}(\mathbf{x})(-\mathbf{f}_p + \frac{1}{2}\nabla|\mathbf{u}|^2 + \mathbf{f})(\mathbf{\Phi}(\mathbf{x}), t)\Delta t\end{aligned} \tag{19}$$

Here, we represent the various pressure terms collectively as $\mathbf{f}_p$ and assume a unified treatment for their path integrals. This approach ensures that our flow-map framework remains compatible with the pressure projection steps of different compressible flow systems. For specific examples of compressible models and their implementations, we refer readers to Section 5. We summarize our compressible flow-map framework in Algorithm 1.

5 Compressible Flow Systems

We implement the unified flow map methodology delineated in the preceding sections to simulate three different compressible flow systems: shallow water, shock wave, and weakly compressible fluid.

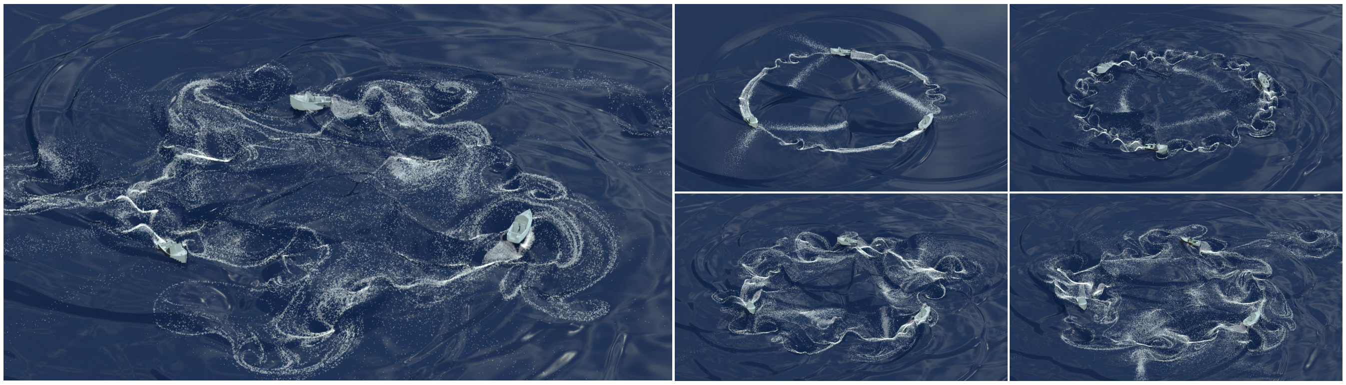

Fig. 3. Three ships moving in a circle on an open ocean surface. Passively advected fluid particles are used to form foams and splashes. Interesting vortical motion marked by foams can be observed.

Algorithm 1 Compressible Flow Map Pipeline

Velocity Mapping: ▷ Sec. 4.3.1
Calculate $\mathbf{u}^M_{s\to t}(\mathbf{x}) = \mathcal{T}^\top_{t\to s}(\mathbf{x})\mathbf{u}_s(\mathbf{\Psi}_{t\to s}(\mathbf{x}))$.
Conservative Quantity Mapping: ▷ Sec. 4.3.2
Calculate $q(\mathbf{x}, t) = |\mathcal{T}_{t\to s}(\mathbf{x})|^\theta q_s(\mathbf{\Psi}(\mathbf{x}, t))$.
Conversion: ▷ Sec. 4.4.1
Convert $\mathbf{u}^M_{s\to t}(\mathbf{x})$ to $\mathbf{u}^A_{t'\to t}(\mathbf{x})$
Pressure Projection: ▷ Sec. 4.4.2
Calculate the pressure term $\mathbf{f}_p$ using conservative quantities $q(\mathbf{x}, t)$ for Acoustic Pressure systems, or directly from $\mathbf{u}^A_{s\to t}(\mathbf{x})$ for Poisson Pressure systems. Then perform projection:

$$\mathbf{u}_t(\mathbf{x}) = \mathbf{u}^A_{s\to t}(\mathbf{x}) - \mathbf{f}_p \Delta t$$

Path Integral Calculation: ▷ Sec. 4.4.3
Update the path integrator as follows:

$$\tilde{\mathcal{E}}_{s\to t}(x) = \tilde{\mathcal{E}}_{s\to t'}(\mathbf{x}) +$$
$$\mathcal{F}^\top_{t\to s}(\mathbf{x})(-\mathbf{f}_p + \frac{1}{2}\nabla|\mathbf{u}|^2 + \mathbf{f})(\mathbf{\Phi}(\mathbf{x}), t)\Delta t$$

5.1 Shallow Water

For incompressible three-dimensional large-scale fluids, such as the ocean surface, where the water depth is much smaller than the horizontal feature size, the vertical momentum equation can be neglected. The shallow water equation can be derived as:

$$\begin{cases} \frac{Dh}{Dt} = -(\nabla \cdot \mathbf{u})h \\ \frac{D\mathbf{u}}{Dt} = -g\nabla h, \end{cases} \tag{20}$$

where $h(\mathbf{x}, t) \geq 0, \mathbf{x} \in \mathbb{R}^2$ is a scalar field representing the vertical height of the water surface above the ground and $\mathbf{u}(\mathbf{x}, t), \mathbf{x} \in \mathbb{R}^2$ is a 2D vector field representing the horizontal velocity.

As a two-dimensional compressible flow system, the height field $h(\mathbf{x}, t)$ and $\ln h(\mathbf{x}, t)$ can be considered analogous to the density field ρ and pressure field p in compressible systems of Equation 6. Following our previous derivation process in section 4 , the solution of the shallow water equation can be expressed using the long-term flow map:

$$\begin{cases} \mathbf{u}(\mathbf{x}, t) = \mathcal{T}^\top_{t\to s}(\mathbf{x})\mathbf{u}_s(\mathbf{\Psi}_{t\to s}(\mathbf{x})) + \mathcal{T}^\top_{t\to s}(\mathbf{x})\tilde{\mathcal{E}}_{s\to t}(\mathbf{\Psi}_{t\to s}(\mathbf{x})), \\ \tilde{\mathcal{E}}_{s\to t}(\mathbf{x}) = \int_s^t \mathcal{F}^T_{s\to\tau}(\mathbf{x})(-g\nabla h + \frac{1}{2}\nabla|\mathbf{u}|^2)(\mathbf{\Phi}_{s\to\tau}(\mathbf{x}), \tau)d\tau, \\ h(\mathbf{x}, t) = |\mathcal{T}_{t\to s}(\mathbf{x})|h_s(\mathbf{\Psi}_{t\to s}(\mathbf{x})), \end{cases} \tag{21}$$

where $\mathbf{\Phi}_{s\to t}$ and $\mathbf{\Psi}_{t\to s}$ are two-dimensional flow maps evolving under the non-divergence-free 2D horizontal velocity $\mathbf{u}(\mathbf{x}, t)$, and the 2×2 matrices $\mathcal{F}_{s\to t}$ and $\mathcal{T}_{t\to s}$ represent Jacobians of $\mathbf{\Phi}_{s\to t}$ and $\mathbf{\Psi}_{t\to s}$ respectively. In the flow map method, the velocity in Equation 21 is computed using the framework for compressible systems outlined in framework 1, where the pressure term is given by $\mathbf{f}_p = g\nabla h$ in the absence of external forces and viscosity. This pressure term $\mathbf{f}_p = g\nabla h$ can be obtained from the height field, mapped by flow maps, as shown in the third lines of Equation 21.

5.2 Shock Wave

5.2.1 Acoustic Pressure Method. Following standard literature [Monaghan and Gingold 1983] and using acoustic pressure methods for simulating compressible flow, we describe the governing equations:

$$\begin{cases} \frac{D\rho}{Dt} = -\rho\nabla \cdot \mathbf{u}, \\ \frac{D\mathbf{u}}{Dt} = -\frac{1}{\rho}\nabla p, \\ \frac{De}{Dt} = -\frac{p}{\rho}\nabla \cdot \mathbf{u} \end{cases} \tag{22}$$

where e represents fluid internal energy and the system is closed with the equation of state (EOS) $p = (\gamma - 1)\rho e$ and with a speed of sound defined as $c = \sqrt{\gamma(\gamma - 1)e}$.

By substituting p with its value from EOS, the last equation of Equation 22 can be written as $\frac{De}{Dt} = -(\gamma-1)e\nabla\cdot\mathbf{u}$. The solution to the above system can be formed into a similar form as Equation 21 using long-term flow map and the advection equation from Equation 16:

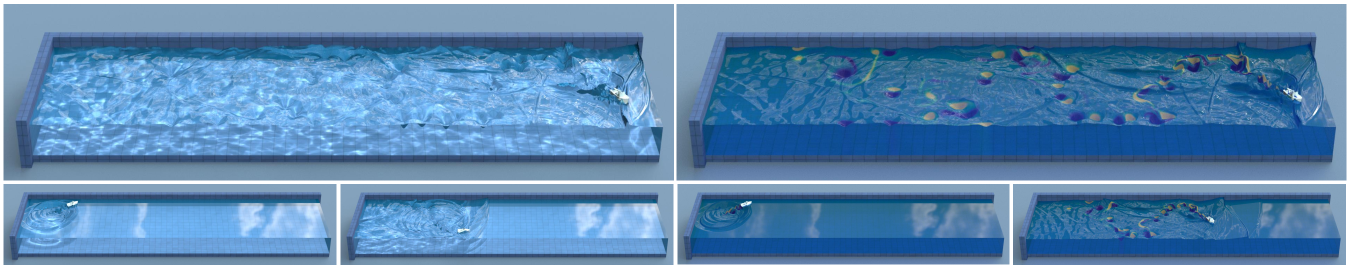

Fig. 4. The lefthand side image shows our simulation rendered in a realistic way. Waves form a caustic effect with vortices forming on the water surface. The righthand side image shows our vorticity rendering directly on the water surface with negative vorticity being purple and positive vorticity being yellow.

$$\begin{cases}\mathbf{u}(\mathbf{x},t)=\mathcal{T}^T_{t\to s}(\mathbf{x})\mathbf{u}_s(\mathbf{\Psi}_{t\to s}(\mathbf{x}))+\mathcal{T}^T_{t\to s}(\mathbf{x})\tilde{\mathcal{E}}_{s\to t}(\mathbf{\Psi}_{t\to s}(\mathbf{x}))\\ \tilde{\mathcal{E}}_{s\to t}(\mathbf{x})=\int_s^t\mathcal{F}^T_{s\to\tau}(\mathbf{x})(-\frac{1}{\rho}\nabla((\gamma-1)\rho e)+\frac{1}{2}\nabla|\mathbf{u}|^2)(\Phi_{s\to\tau}(\mathbf{x}),\tau)d\tau\\ \rho(\mathbf{x},t)=|\mathcal{T}_{t\to s}(\mathbf{x})|\rho_s(\Psi_{t\to s}(\mathbf{x}))\\ e(\mathbf{x},t)=|\mathcal{T}_{t\to s}(\mathbf{x})|^{\gamma-1}e_s(\Psi_{t\to s}(\mathbf{x}))\end{cases} \tag{23}$$

The pressure term now is represented with the EOS constraint which is written as $f_p=\frac{1}{\rho}\nabla((\gamma-1)\rho e)$ and other flow map quantities are defined the same as the previous definition.

5.2.2 Pressure Poisson Method. Solving a compressible system following Poisson projection requires minimal modification to the above system. We follow the definition from [Kwatra et al. 2009] and describe our governing equation as follows:

$$\begin{cases}\frac{D\rho}{Dt}=-\rho\nabla\cdot\mathbf{u},\\ \frac{D\mathbf{u}}{Dt}=-\frac{1}{\rho}\nabla p,\\ \frac{DE}{Dt}=-E\nabla\cdot\mathbf{u}-\nabla\cdot(p\mathbf{u}),\end{cases} \tag{24}$$

Here, E denotes fluid total energy per unit volume and is represented as $E=\rho e+\frac{1}{2}\rho|\mathbf{u}|^2$ where e denotes the internal energy, and the second term represents kinetic energy. The system is closed with an equation of state (EOS) $p=(\gamma-1)\rho e$. Following [Kwatra et al. 2009], we split the above system into advective and non-advective parts and couple them with the Mach Poisson projection. By rewriting the advection part for E and ρ as:

$$\begin{cases}\frac{D\rho}{Dt}&=-\rho\nabla\cdot\mathbf{u},\\ \frac{DE}{Dt}&=-E\nabla\cdot\mathbf{u},\end{cases} \tag{25}$$

we solve this system directly with RK4 advection scheme and get E^A_t,ρ^A_t. The velocity advection remains unchanged using the flow map method which is calculated as $\mathbf{u}^A_t=\mathcal{T}^\top_{t\to s}(\mathbf{x})\mathbf{u}_s(\mathbf{\Psi}_{t\to s}(\mathbf{x}))+\mathcal{T}^\top_{t\to s}(\mathbf{x})\tilde{\mathcal{E}}_{s\to t}(\mathbf{\Psi}_{t\to s}(\mathbf{x}))$

In order to capture shocks while using a large CFL number, Mach Poisson was proposed. Discretizing the second equation in Equation 24, we have $\mathbf{u}_t-\mathbf{u}^A_t=\Delta t\frac{\nabla p_t}{\rho_t}$. Taking divergence on both sides leaves an additional $\nabla\cdot\mathbf{u}_t$ term due to compressibility of fluid which can be estimated using advected pressure field [Kwatra et al. 2009] as $\nabla\cdot\mathbf{u}_t=\frac{p^A_t-p_t}{\Delta t\rho_{r-1}c_{r-1}}$ Using this estimated divergence term and taking divergence on both sides of the previous equation, the Poisson equation becomes:

$$\frac{p^A_t}{\rho_{t'}(c^2_{t'})\Delta t^2}-\frac{1}{\Delta t}\nabla\cdot\mathbf{u}^A_t=-\frac{\nabla^2 p_t}{\rho_t}+\frac{p_t}{\Delta t^2c^2_{t'}\rho_{t'}} \tag{26}$$

Here, p^A denotes the advected pressure which is reinitialized every step using the EOS equation to avoid numerical drift and is advected using RK4 scheme with $\frac{Dp}{Dt}=0$. $\rho_{t'}$ represents the ρ from previous step, c denotes sound speed. Other quantities here are described in previous sections.

After solving the Poisson equation,

$$\mathbf{f}_p=\frac{1}{\rho_t}\nabla p_t \tag{27}$$

is used for projecting velocity using Equation 18.

After solving Mach Poisson, we perform the correction step in [Kwatra et al. 2009]. We first split pressure from cell center to cell faces using a density-weighted averaging and then update $\rho\mathbf{u}$ with $(\rho\mathbf{u})_t=(\rho\mathbf{u})^A_t-\Delta t\frac{p^{i+1/2}_t-p^{i-1/2}_t}{\Delta x}$ and interpolates back to cell faces by dividing the average density on cell faces. The split velocity is then multiplied by split pressure on cell faces to get $(p\mathbf{u})_t$ with updates E through $E_t=E^A_t-\Delta t\nabla\cdot(p\mathbf{u})_t$. Finally, we calibrate pressure field f_{p_t} with EOS equation using the updated E_t and $\mathbf{u}_t$ and ρ_t as: $p_t=(\gamma-1)(E_t-(0.5\rho_t|\mathbf{u}_t|^2))$ and use this pressure for caliberation of $\mathbf{f}_p=\frac{1}{\rho_t}\nabla p_t$ The solution to the system is closed with

$$\tilde{\mathcal{E}}_{s\to t}(\mathbf{x})=\int_s^t\mathcal{F}^\top_{s\to\tau}(-\mathbf{f}_p+\frac{1}{2}\nabla|\mathbf{u}|^2)(\mathbf{\Phi}_{s\to\tau}(\mathbf{x}),\tau)d\tau.$$

5.3 Weakly Compressible Fluids

Our method also supports the simulation of weakly compressible fluid systems, which can be regarded as compressible shock wave systems without considering the energy equation, and governed by the equation of state $p=p_0\left(\left(\frac{\rho}{\rho_0}\right)^\gamma-1\right)$ with a relatively large p_0 [Becker and Teschner 2007]. As a result, the system can still be computed using a procedure similar to that in Equation 23, with a weakly compressible EOS.

6 Time Integration

We outline our time integration scheme below:

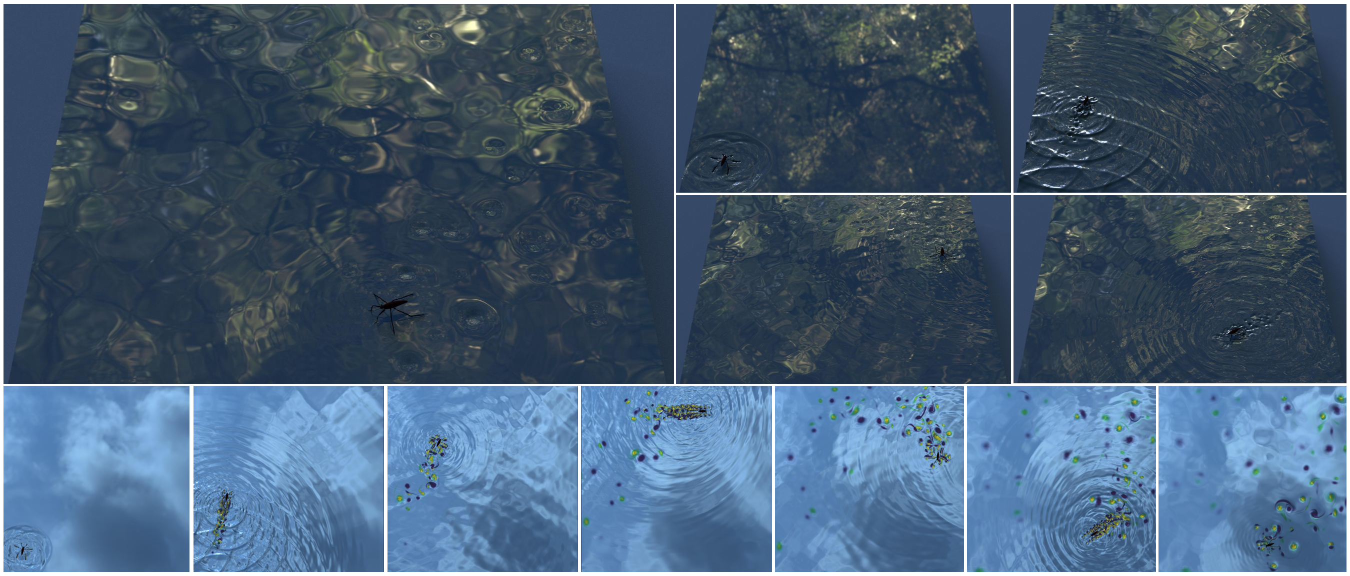

Fig. 5. We simulate a water strider jumping in a water pond. We observed interesting surface wave patterns together with vortices created due to the motion of the water strider.

(1) **Reinitialization**. After every n steps, flow maps are set to current position with $\mathcal{F}_{s\to t}$ and $\mathcal{T}_{t\to s}$ reset to $\mathcal{I}$. Buffers $\tilde{\mathcal{E}}_{s\to t}$ are set to 0. If PFM is used, particles are reinitialized following [Zhou et al. 2024]. If EFM is used, the velocity buffer used for evolution is emptied.
(2) **CFL Condition**. Δt is computed based on the fluid velocity field, the gradient of the pressure field, and the CFL number following [Kwatra et al. 2009] when calculating shock waves. If simulating Shallow Water, we use the CFL condition following [Jeschke and Wojtan 2023].
(3) **Midpoint Method**. We adopt a leapfrog-style temporal integration scheme to enhance conservation of physical quantities, following [Deng et al. 2023]. Advection is performed using RK4 on the grid, while pressure is computed either via the Acoustic Pressure methods (Eqs. 21, 23) or through the Mach Poisson Projection (Equation 26).
(4) **Advection**. We march $\mathcal{T}_{t\to s}$ and $\mathcal{F}_{s\to t}$ following flow map gradient update Equation 3 if using PFM and Equation 4 if using EFM. p, E and ρ are advected following either Equations 21 and 23 for **Acoustic Pressure** methods described in Section 5.2 and Section 5.1 or Equation 25 as detailed in Section 5.2.2 for **Pressure Poisson** method. All of our advection scheme uses **RK4** for advection following the algorithm listed in [Deng et al. 2023] with divergence and gradient terms are calculated following [Jiang et al. 2016] using:
$$\nabla \cdot \mathbf{u}^p = \sum_{i\in N_p} \mathbf{u}_i \cdot \nabla w_{ip} \tag{28}$$
$$\nabla \mathbf{u}^p = \sum_{i\in N_p} \mathbf{u}_i \nabla w_{ip}, \tag{29}$$
where w_{ip} is the quadratic weight, and N_p is the set of grid points i neighboring particle p.
(5) **Impulse to Velocity Conversion**. We compute $\nabla \mathbf{u}_t$ with $\mathbf{u}_{mid}$ using the equation above. $\mathbf{u}_t^A$ is then computed with $\tilde{\mathcal{E}}_{s\to t}$, $\mathbf{u}_{\text{mid}}$ and $\mathbf{m}_s$ prescribed in Equation 17.
(6) **Pressure Enforcement** Pressure enforcement in different compressible systems are detailed in section 5. If a **Acoustic Pressure** pressure enforcement is used, pressure calculated using $\mathbf{f}_p = g\nabla h$ or $\mathbf{f}_p = \frac{1}{\rho}\nabla((\gamma-1)\rho e)$ and enforced using $\mathbf{u}_t = \mathbf{u}_t^A - \mathbf{f}_p \Delta t$ following Equation 18. If **Pressure Poisson** pressure enforcement is used, $\mathbf{f}_p$ is calculated through solving Equation 26 and calculated with Equation 27. Pressure is enforced in the same way as Equation 18.
(7) **Non-Advective Calculation** If **Pressure Poisson** is used, an additional non-advective caliberation is applied. Procedures directly follow from the last paragraph of Sec. 5.2.2. **Acoustic Pressure** methods do not need this step.
(8) **Buffer Update**. We update $\tilde{\mathcal{E}}_{s\to t}$ according to Equation 19. External forces like gravity $\rho\mathbf{g}$ are added to the grid and added to the buffer.

7 Visualization

Shallow Water. To enhance wave visualization in shallow water simulations, we apply a fake caustic effect by adding an underwater light source whose intensity is proportional to $|\nabla h|$, the gradient norm of the height field. This mimics underwater light refraction patterns, as used in Fig. 4. To highlight vortex dynamics, surface vorticity is also rendered, as shown in Fig. 8.

Shock Wave. To visualize shock and turbulence across varying flow regimes, we render $|\nabla p|$, the norm of the pressure gradient. This quantity captures both weak pressure fluctuations at subsonic

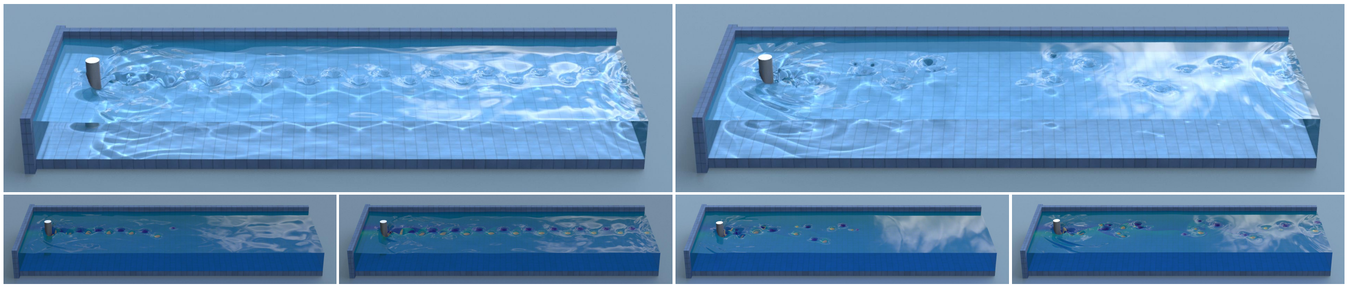

Fig. 6. We show a static pillar creating Karman Vortex Street on the left-hand side figure and a passively moving pillar forming a different pattern on the right-hand side. We visualize the flow using realistic caustics (top row) and vorticity coloring (bottom row).

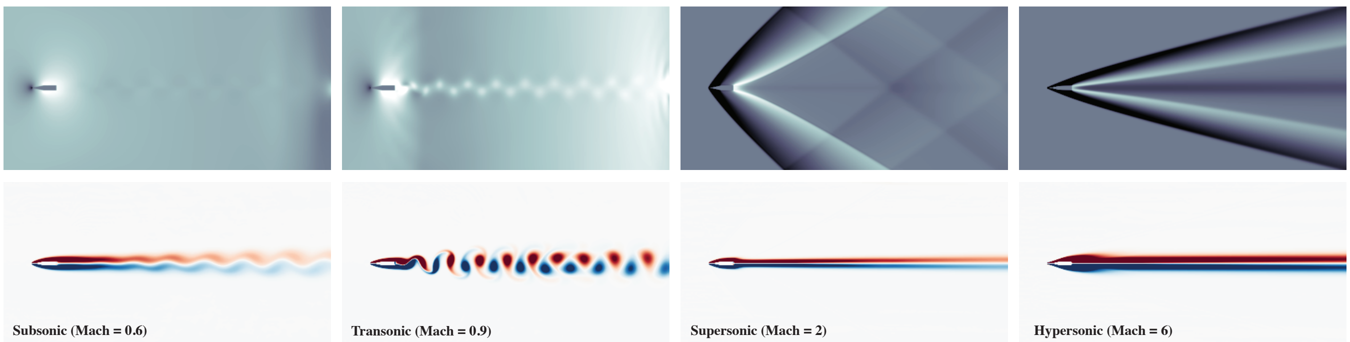

Fig. 7. Bullets are simulated with speed ranging from subsonic to hypersonic. The shock wavefront and expansion fan are clearly visualized. Vortices are created at the tail of the bullet below sound speed.

speeds and sharp fronts at supersonic or hypersonic speeds. Visualizing $|\nabla p|$ volumetrically and applying thresholds allows simultaneous depiction of turbulence and shock structures.

8 Validation

8.1 Shallow Water

We compare our method against prior Shallow Water approaches, including semi-Lagrangian (SL), advanced Euler (AE) with advection from [Jeschke and Wojtan 2023], and APIC [Jiang et al. 2015]. All methods use our Acoustic Pressure Penalty formulation and are prefixed with "AP."

8.1.1 Free-surface Surface Vortices. We initialize surface vortices in a $[0, 1]^2$ domain at 512×512 resolution. In Fig.11 (right), three same-spin vortices form an equilateral triangle; in Fig.11 (left), two are placed at $(0.4, 0.5)$ and $(0.6, 0.5)$. With no viscosity, ideal conditions should preserve vorticity. Our method maintains vortex rotation significantly longer than others, which dissipate rapidly.

8.1.2 Free-surface Leapfrog. Figure 12 shows a classical vortex preservation test using standard leapfrog settings from prior work [Deng et al. 2023; Nabizadeh et al. 2022; Zhou et al. 2024]. We simulate this under a compressible flow in a 1024×512 domain. Our method preserves vortices without enforcing divergence-free constraints, unlike prior shallow water methods which dissipate quickly.

8.1.3 Free-surface Karman Vortex Street. Experiments [Han et al. 2024; Rueckner 2012] show that Karman vortex streets can form on water surfaces via either constant-speed object motion or two-way object-fluid coupling. Inspired by these, we set up two simulations. In Fig. 6 (left), a static cylinder in uniform flow generates a vortex street. In Fig. 6 (right), a coupled cylinder responds to incoming flow, producing distinct patterns. Both use a 1536×512 domain.

8.2 Compressible Flow

In our compressible flow experiments, we evaluate the effectiveness of our flow map advection by comparing it with semi-Lagrangian (SL) and Affine Particle-in-Cell (APIC) [Jiang et al. 2015] under shock test conditions. Methods are prefixed by the pressure solver used: "AP" for Acoustic Pressure and "M" for Mach Poisson. For example, "MSL" uses Mach Poisson with SL advection, while "APSL" uses Acoustic Pressure with SL. We benchmark against MWENO, a Mach Poisson method using a TVD-WENO scheme [Cao et al. 2022; Kwatra et al. 2009].

8.2.1 1D Sod Tube Test. We validate shock discontinuity using the classical Sod test with an initial staircase distribution:

$$(\rho(\mathbf{x}, 0), u(\mathbf{x}, 0), p(\mathbf{x}, 0)) = \begin{cases} (1, 0, 1) & \text{if } \mathbf{x} \leq 0.5, \\ (0.125, 0, 0.1) & \text{if } \mathbf{x} > 0.5, \end{cases} \tag{30}$$

in the domain $[0, 1]$. As shown in Fig. 14a, our result closely matches the MWENO reference solution. Compared with other methods

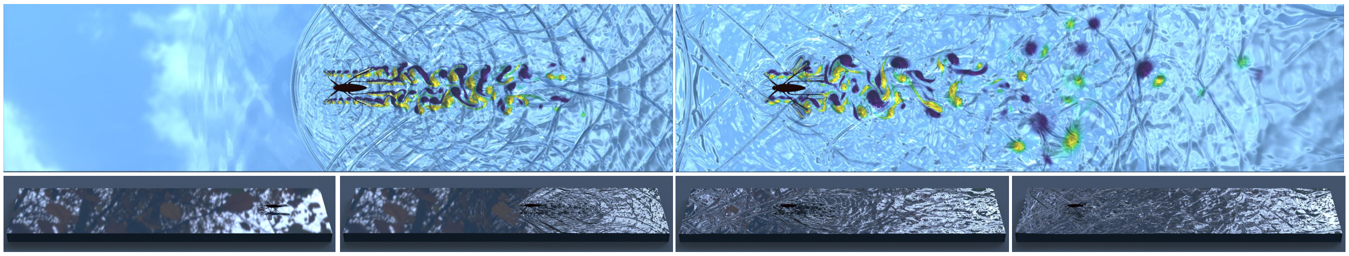

Fig. 8. A water strider jumping in a rectangular domain. Results on the top row show high alignment with real experiment photos in [Mackenzie 2006].

without using flow maps for velocity advection and only a single-step advection of flow map gradient under fluid simulation scenarios, such as APIC and semi-Lagrangian methods, our method preserves the shock propagation speed.

8.2.2 2D Circular Shock Test. Following [Kwatra et al. 2009], we set up the initial condition prescribed as:

$$(\rho, u, v, p) = \begin{cases} (1, 0, 0, 1) & \text{if } r \le 0.4, \\ (0.125, 0, 0, 0.1) & \text{if } r > 0.4. \end{cases} \tag{31}$$

Here, $r = \sqrt{x^2 + y^2}$ where x, y are the coordinate of grid cell center in a $[0,1]^2$ domain. Our method indicates well resolved shocks with alignment to the referenced solution (MWENO) as shown in Fig. 14b. Other methods dissipate quickly even using the mapped density and energy with our method.

8.2.3 2D Bullet under Different Mach Numbers. Figure 7 shows simulations of bullets traveling at different speeds in a 1024×512 domain. Snapshots are captured after shock convergence. The incoming fluid Mach numbers are 0.4 (subsonic), 0.9 (transonic), 2 (supersonic), and 6 (hypersonic), matching experimental observations in [Snow 1967]. Vorticity behind subsonic bullets is also visualized, highlighting our method's ability to resolve both shocks and vortical structures.

8.2.4 3D Piston Leapfrog. To further validate our method's ability to handle compressible flow while preserving vorticity, we adapt the classical 3D Leapfrog test—originally for incompressible flows [Deng et al. 2023; Nabizadeh et al. 2022; Zhou et al. 2024]—by introducing a piston moving at speed 0.15. As shown in Fig. 19, our method captures both the energy increase and the persistence of distinct vortex rings until they reach the wall. In contrast, other methods show early diffusion, merging, or inaccurate energy dynamics.

9 Ablation Study

9.1 Necessity of Flow Map dependent advection

As shown in Equation 16, the advection of E and ρ can be directly calculated using the advection term from each step. We call such calculated value an advected value. Here, we study the necessity of using our flow map mapped value to achieve the desired accuracy in the shock wave test. We use the 1D sod tube test as the example for demonstration as shown in Fig. 16.

In Fig. 17, we show that using Eq. 10 and Eq. 12 will give identical result using the classical Sod Tube test in compressible flow. This experiment justifies our choice of using the form (Eq. 12) that is identical to incompressible flow map simulations which enables better unification of the framework.

10 Results

The following sections demonstrate our method applied to a range of fluid phenomena. All simulations were performed on an NVIDIA RTX 4090 GPU (24GB) using Taichi [Hu et al. 2019]. We adopt CFL conditions from [Kwatra et al. 2009] for shock waves and [Jeschke and Wojtan 2023] for SWE. A CFL number of 0.5 is used in line with common practice in EFM/PFM flow-map literature, while a more conservative CFL (0.25) is applied in extreme cases, such as Mach 6 shocks or SWE scenarios with splash particles (Fig. 21, Fig. 20, Fig. 3).

Setup parameters are detailed in Table 1. Frame time (including I/O) is averaged across the simulation, as CFL conditions lead to variable time steps. Simulations were completed within 1–12 hours, with Trefoil (Fig. 13) being the fastest and Ship in Tank (Fig. 4) the most computationally intensive. Most cases finished in 4–7 hours, with bottlenecks primarily in buffer evaluation, particle-to-grid transfers, and high-resolution `.exr` output for rendering.

10.1 Shallow Water

We demonstrate a range of phenomena simulated using our shallow water solver. Solid boundaries are treated with an immersed boundary method, where prescribed solid velocities exert one-way coupling on the fluid.

10.1.1 Ship In Tank. Figure 4 shows a ship moving along a sinusoidal path, aligned tangentially. Simulated in a 6×1.5 domain at 3600×900 resolution, the motion generates surface waves and complex vortices.

10.1.2 Pillars. As shown in Fig. 21, we simulate wave interaction with static pillars, mimicking sea harbor scenes. In a 900×1800 domain, incoming waves generate sprays, foams, and vortices around the pillars due to flow-solid interaction.

10.1.3 Swimming Board. In Fig. 20, three boards traverse a 1000×800 domain at constant speed while swinging, mimicking fish-like

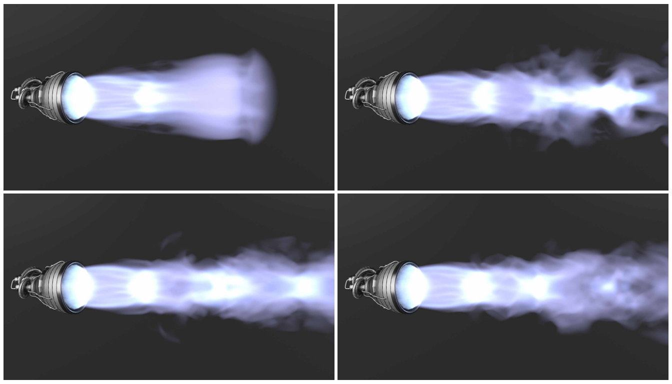

Fig. 9. We simulate the Mach diamond phenomenon, formed by a supersonic jet exiting a nozzle and producing a distinct pattern of pressure concentrations.

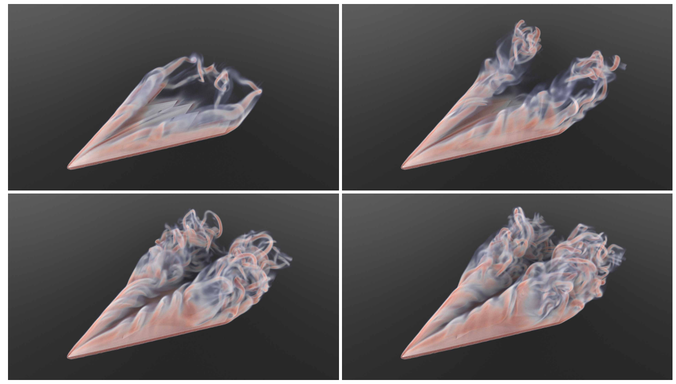

Fig. 10. We simulate a Delta Wing at an angle of attack of 20 degrees. Vortices are formed in the same fashion as reported in [Délery 2001].

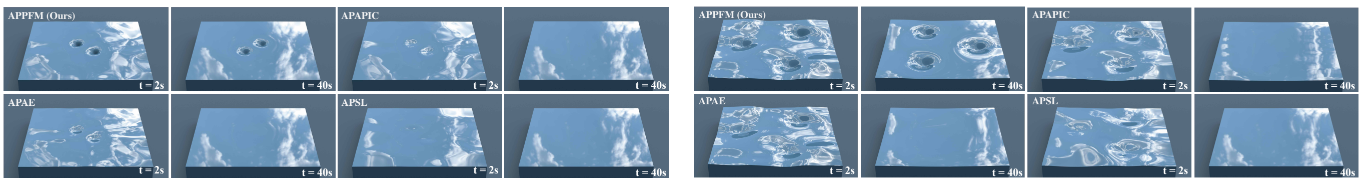

Fig. 11. We show the experiment of simulating two/three surface vortices. Snapshots at frames 10 and 200 are captured. Our method successfully preserves vortices on the water surface but under other methods they diffuse quickly.

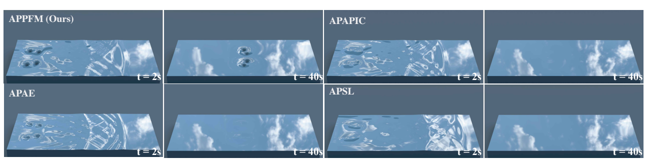

Fig. 12. We perform a surface leapfrog experiment and show our method successfully keeps the leapfrogging behavior while others cannot.

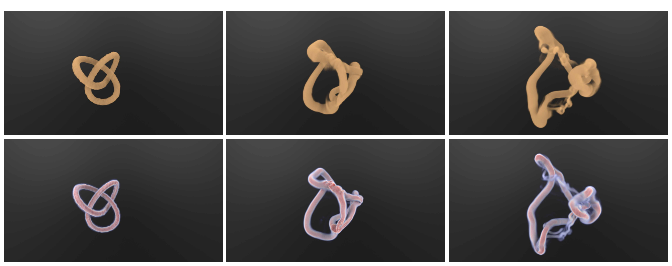

Fig. 13. We perform a classical test case for vorticity preservation under incompressible flow using our compressible flow map solver. Results align with what is shown in [Kleckner and Irvine 2013].

motion. This produces waves at the head and Karman vortices behind, consistent with prior studies [Hieber and Koumoutsakos 2008].

10.1.4 Three Ships On The Sea. Figure 3 shows three boats moving along a circular path in a domain of size 3 with 1800×1800 resolution. Their motion generates interacting vortices, splashes, and complex surface wave patterns.

10.1.5 Water Strider. We simulate water striders moving on a shallow surface using prescribed motions from Blender as input to the immersed boundary method. Surface tension is omitted for simplicity. The resulting vortices closely resemble those observed in nature and experiments [Hu et al. 2003]. Fig. 5 shows a simulation in a 3×3 domain at 1800×1800 resolution with $\Delta t = 0.0003$, while Fig. 8 shows a 6×1.5 domain at 3600×900 resolution with $\Delta t = 0.0001$.

10.2 Compressible Flow

We simulate shock wave phenomena relevant to aerospace scenarios. Jet speeds are set to realistic values—supersonic for aircraft and hypersonic for rockets. All experiments use a $400\times200\times200$ domain.

10.2.1 3D Jet. Figure 15 shows jets flying at Mach 0.6 and Mach 2. At low Mach with a 15-degree angle of attack, vortices form above the wings due to lift-induced flow separation.

10.2.2 3D Mach Diamond. In Fig. 9, we simulate 3D Mach diamonds—shock structures formed by supersonic jets exiting nozzles into ambient air. Our method captures the characteristic pattern of shock waves and expansion fans in this classic compressible flow setup.

10.2.3 Dragon Capsule On Mars. Figure 2 shows a SpaceX Dragon capsule landing on Mars at Mach 0.4, 0.9, and 2. The shock structures at Mach 2 closely match those reported in [Spa 2015].

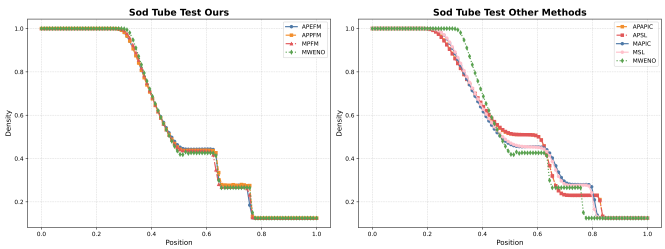

(a) 1D sod tube test. Our result is comparable to that of MWENO.

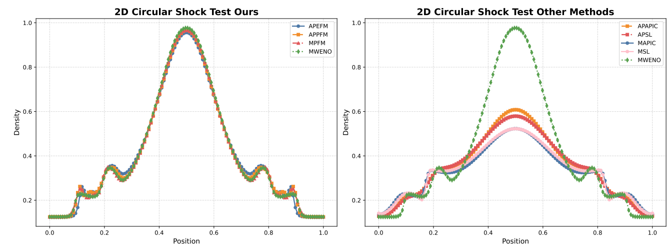

(b) 2D circular shock test. Our result highly aligns with the reference solution using MWENO.

Fig. 14. Validation of shock wave tests using various methods: APSL (Acoustic Pressure + semi-Lagrangian), MSL (Mach Poisson + semi-Lagrangian), APAPIC (Acoustic Pressure + APIC), MAPIC (Mach Poisson + APIC), APPFM (Acoustic Pressure + PFM), APEFM (Acoustic Pressure + EFM), MPFM (Mach Poisson + PFM), and MWENO (Mach Poisson + TVD-WENO).

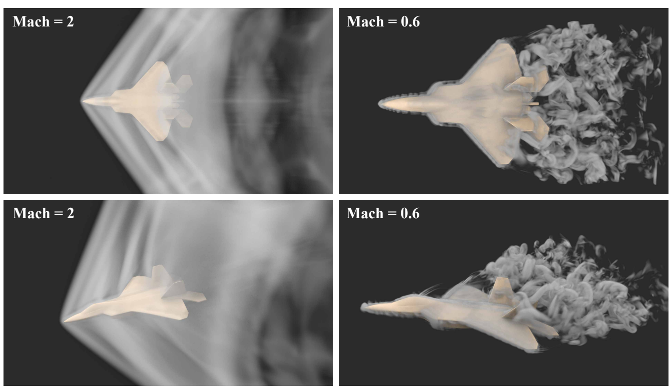

Fig. 15. We simulate a jet breaking sound barrier on the left figures. On the right figures, we show vortices forming during its climbing process, i.e. simulated with an angle of attack.

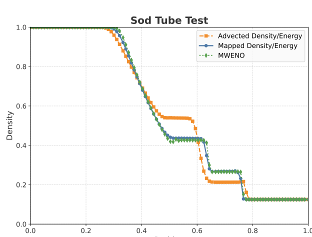

Fig. 16. We show that without using flow map for advection, shock wave can not be resolved correctly.

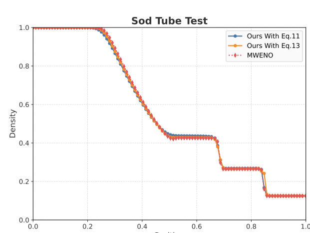

Fig. 17. We show that using Eq. 10 and Eq. 12 does not affect the accuracy of our method.

10.2.4 3D Rocket. In Fig. 18, we simulate a rocket ascending at Mach 0.4 to 6, spanning subsonic to hypersonic speeds. The results demonstrate our method's ability to handle strong shocks and high compressibility.

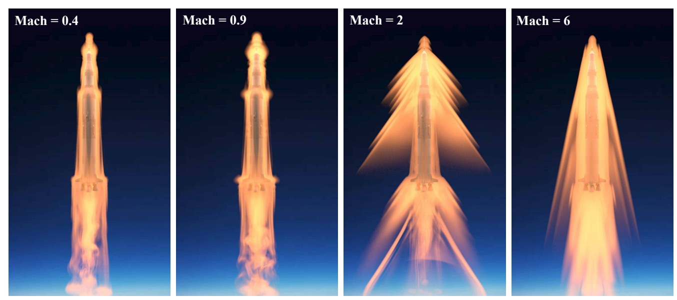

Fig. 18. We show a rocket launching and accelerating from mach 0.4 to mach 6. The extreme ratio of compression is simulated allowing visualization of a hypersonic shock wave front. Vortical patterns can be observed at relatively low speeds.

10.3 Weakly Compressible Flow

We present results across three representative cases: vortex shedding from a delta wing, trefoil vortex preservation, and ink drop dynamics with viscous forces. All simulations use a $256 \times 128 \times 128$ resolution.

10.3.1 Ink Drop. Our method integrates prior flow map research and supports external force modeling via the force buffer in [Li et al. 2024b]. Figure 22 shows complex ink ring formation and breakup, demonstrating our method's capacity for handling viscosity-dominated flows.

Fig. 22. We simulate an ink drop forming a complex structure under the influence of viscosity.

10.3.2 Delta Wing. We simulate a delta wing at a 20-degree angle of attack and Mach 0.6. The results match experimental observations in [Délery 2001].

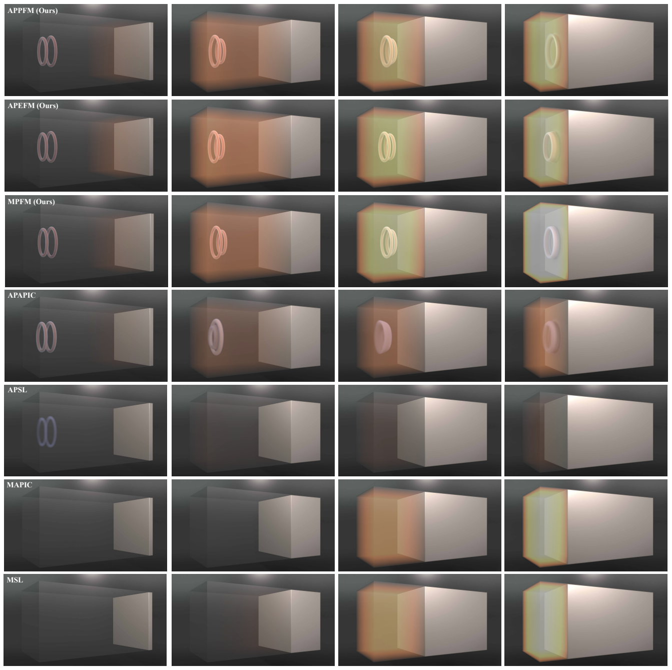

Fig. 19. Comparison of vorticity preservation under compressible flow induced by piston motion. Simulations are conducted using: APSL (Acoustic Pressure + semi-Lagrangian), MSL (Mach Poisson + semi-Lagrangian), APAPIC (Acoustic Pressure + APIC), MAPIC (Mach Poisson + APIC), APPFM (Acoustic Pressure + PFM), APEFM (Acoustic Pressure + EFM), and MPFM (Mach Poisson + PFM). Energy and vorticity fields are visualized with the piston moving at constant speed.

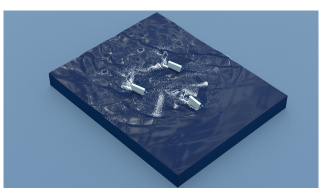

Fig. 20. Three boards swimming at constant speed

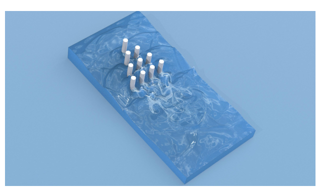

Fig. 21. We simulate pillars confronting incoming waves.

10.3.3 Trefoil. Figure 13 shows a trefoil vortex preservation test, initialized as in [Nabizadeh et al. 2022]. Our results align with experiments by Kleckner and Irvine [2013], confirming accurate vorticity evolution.

11 Conclusion

This study expands flow-map methodologies to effectively simulate high-Mach-number, free surface fluid represented as height fields and weakly compressible flows, significantly broadening the scope of these techniques beyond their traditional incompressible focus. Through a unified model based on Lagrangian path integrals, our framework handles a diverse array of phenomena. Our findings demonstrate the framework's ability to preserve and evolve complex fluid dynamics, showcasing the potential for broader applications in computational physics and computer graphics.

Discussion with compressible impulse. We begin by relating our method to prior formulations of the compressible impulse variable in computational physics [Pareja 2007; Shivamoggi 2010]. The impulse gauge is defined as $\mathbf{m}_t = \mathbf{u}_t + \frac{1}{\rho_t}\nabla\tilde{\Lambda}_t$, where ρ_t is time-dependent and spatially varying. Under the barotropic condition with time-invariant density ($\partial\rho/\partial t = 0$), Pareja [2007]; Shivamoggi [2010] showed that $\mathbf{m}_t(\mathbf{x}) = \mathcal{T}_{t\to s}^{\top}(\mathbf{x})\mathbf{u}_s(\mathbf{\Psi}_{t\to s}(\mathbf{x}))$ still holds. However, no generalization was provided for non-barotropic cases. To enable our flow map framework to capture a broader class of compressible flows, we revisit this derivation and develop a formulation that holds without restrictive assumptions.

Limitation. For our boundary conditions used in the examples, we left them untreated for the Acoustic Pressure method, i.e., mimicking the air pressure boundary condition and setting to air boundary in Mach Poission. However, small reflected waves can still be observed where absorption boundary conditions for waves are not easy to implement. In electromagnetic wave simulations, such a boundary condition is termed the Perfect Matching Layer and still remains an active research area [Berenger 1996]. In the graphics community, [Chern 2019] proposed a method for absorption layers but this is beyond the scope of this paper.

Future Work. Previous paper on compressible flow often incorporates solid-fluid coupling [Cao et al. 2022; Hyde and Fedkiw 2019; Kwatra et al. 2009], however, a monolithic coupling framework using a flow map is still an unsolved problem that motivates ongoing research. We believe a monolithic coupling framework will greatly open the possible phenomena that our method can simulate.

Acknowledgments

We express our gratitude to the anonymous reviewers for their insightful feedback. We also thank Yuchen Sun, Sinan Wang and Mengdi Wang for their insightful discussion. Georgia Tech authors also acknowledge NSF IIS #2433322, ECCS #2318814, CAREER #2420319, IIS #2433307, OISE #2433313, and CNS #1919647 for funding support. We credit the Houdini education license for video animations.

Sandia National Laboratories is a multi-mission laboratory managed and operated by National Technology & Engineering Solutions of Sandia, LLC (NTESS), a wholly owned subsidiary of Honeywell International Inc., for the U.S. Department of Energy's National Nuclear Security Administration (DOE/NNSA) under contract DE-NA0003525. This written work is authored by an employee of NTESS. The employee, not NTESS, owns the right, title and interest in and to the written work and is responsible for its contents. Any subjective views or opinions that might be expressed in the written work do not necessarily represent the views of the U.S. Government. The publisher acknowledges that the U.S. Government retains a non-exclusive, paid-up, irrevocable, world-wide license to publish or reproduce the published form of this written work or allow others to do so, for U.S. Government purposes. The DOE will provide public access to results of federally sponsored research in accordance with the DOE Public Access Plan.

Table 1. This table gives detailed simulation settings of the major example. For total frames, we list the total frame numbers we used in each video in the supplemental material. Note that the timing for frames is an average; frame times varied due to CFL-based time stepping.

Example	Resolution	Flow Map Length	Time (sec / substep)	Time (sec / frame)	Total Frames	Total Time (hour)
Mach 0.4, 0.9, 2 Bullet	1024 × 512	30	0.15	4 / 6 / 20	400	0.4 / 0.7 / 2.2
Mach 6 Bullet	1024 × 512	20	0.15	48	200	2.7
Mach 0.4, 0.9, 2 Rocket	400 × 200 × 200	8	0.77	35 / 43 / 69	400	3.9 / 4.8 / 7.6
Mach 6 Rocket	400 × 200 × 200	5	0.77	149	200	8.3
3D Jet	400 × 200 × 200	15	0.82	61	400	6.8
Mach 0.4, 0.9, 2 Dragon Capsule	400 × 200 × 200	8	0.77	35 / 42 / 69	400	3.9 / 4.7 / 7.7
Trefoil	128 × 128 × 128	15	0.44	20	200	1.1
Delta Wing	256 × 128 × 128	8	0.60	28	400	3.1
Ink	256 × 128 × 128	8	0.52	24	650	4.3
Three Ships On The Sea	1800 × 1800	50	<0.1	42	800	9.3
Ship in Tank	3600 × 900	70	<0.1	70	650	12.6
Pillars	900 × 1800	40	<0.1	84	400	9.3
Swimming Board	1000 × 800	40	<0.1	30	500	4.1
Water Strider (Square)	1800 × 1800	150	<0.1	9	1800	4.5
Water Strider (Rectangular)	3600 × 900	80	<0.1	26	960	6.9

References

2015. GPUs to Mars: Full-Scale Simulation of SpaceX's Mars Rocket Engine. https://youtu.be/vYA0f6R5KAI?feature=shared.

George Biddell Airy. 1845. *Tides and waves*. B. Fellowes.

Markus Becker and Matthias Teschner. 2007. Weakly compressible SPH for free surface flows. In *Proceedings of the 2007 ACM SIGGRAPH/Eurographics symposium on Computer animation*. 209–217.

J-P Berenger. 1996. Perfectly matched layer for the FDTD solution of wave-structure interaction problems. *IEEE Transactions on antennas and propagation* 44, 1 (1996), 110–117.

Leigh Brookshaw. 1985. A method of calculating radiative heat diffusion in particle simulations. *Publications of the Astronomical Society of Australia* 6, 2 (1985), 207–210.

Yadi Cao, Yunuo Chen, Minchen Li, Yin Yang, Xinxin Zhang, Mridul Aanjaneya, and Chenfanfu Jiang. 2022. An efficient b-spline lagrangian/eulerian method for compressible flow, shock waves, and fracturing solids. *ACM Transactions on Graphics (TOG)* 41, 5 (2022), 1–13.

Duowen Chen, Zhiqi Li, Junwei Zhou, Fan Feng, Tao Du, and Bo Zhu. 2024. Solid-Fluid Interaction on Particle Flow Maps. *ACM Transactions on Graphics (TOG)* 43, 6 (2024), 1–20.

Jim X Chen, NDV Lobo, Charles E Hughes, and J Michael Moshell. 1997. Real-time fluid simulation in a dynamic virtual environment. *IEEE Computer Graphics and Applications* 17, 3 (1997), 52–61.

Shiyi Chen and Gary D Doolen. 1998. Lattice Boltzmann method for fluid flows. *Annual review of fluid mechanics* 30, 1 (1998), 329–364.

Nuttapong Chentanez and Matthias Müller. 2010. Real-time Simulation of Large Bodies of Water with Small Scale Details.. In *Symposium on Computer Animation*. 197–206.

Nuttapong Chentanez, Matthias Müller, and Tae-Yong Kim. 2015. Coupling 3D Eulerian, heightfield and particle methods for interactive simulation of large scale liquid phenomena. *IEEE transactions on visualization and computer graphics* 21, 10 (2015), 1116–1128.

Albert Chern. 2019. A reflectionless discrete perfectly matched layer. *J. Comput. Phys.* 381 (2019), 91–109.

Ricardo Cortez. 1996. An impulse-based approximation of fluid motion due to boundary forces. *J. Comput. Phys.* 123, 2 (1996), 341–353.

Keenan Crane, Fernando de Goes, Mathieu Desbrun, and Peter Schröder. 2013. Digital geometry processing with discrete exterior calculus. In *ACM SIGGRAPH 2013 Courses* (Anaheim, California) *(SIGGRAPH '13)*. Association for Computing Machinery, New York, NY, USA, Article 7, 126 pages. https://doi.org/10.1145/2504435.2504442

B De St Venant. 1871. Theorie du mouvement non-permanent des eaux avec application aux crues des rivers et a l'introduntion des Marees dans leur lit. *Academic de Sci. Comptes Redus* 73, 99 (1871), 148–154.

Jean M Délery. 2001. Robert Legendre and Henri Werlé: toward the elucidation of three-dimensional separation. *Annual review of fluid mechanics* 33, 1 (2001), 129–154.

Yitong Deng, Hong-Xing Yu, Diyang Zhang, Jiajun Wu, and Bo Zhu. 2023. Fluid Simulation on Neural Flow Maps. *ACM Transactions on Graphics (TOG)* 42, 6 (2023), 1–21.

Ronald P Fedkiw, Guillermo Sapiro, and Chi-Wang Shu. 2003. Shock capturing, level sets, and PDE based methods in computer vision and image processing: a review of Osher's contributions. *J. Comput. Phys.* 185, 2 (2003), 309–341.

Yue Gao, Chen-Feng Li, Shi-Min Hu, and Brian A Barsky. 2009. Simulating gaseous fluids with low and high speeds. In *Computer Graphics Forum*, Vol. 28. Wiley Online Library, 1845–1852.

Jón Tómas Grétarsson and Ron Fedkiw. 2013. Fully conservative leak-proof treatment of thin solid structures immersed in compressible fluids. *J. Comput. Phys.* 245 (2013), 160–204.

Jón Tómas Grétarsson, Nipun Kwatra, and Ronald Fedkiw. 2011. Numerically stable fluid–structure interactions between compressible flow and solid structures. *J. Comput. Phys.* 230, 8 (2011), 3062–3084.

Toshiya Hachisuka. 2005. Combined Lagrangian-Eulerian approach for accurate advection. In *ACM SIGGRAPH 2005 Posters*. 114–es.

Trond Runar Hagen, Jon M Hjelmervik, K-A Lie, Jostein R Natvig, and M Ofstad Henriksen. 2005. Visual simulation of shallow-water waves. *Simulation Modelling Practice and Theory* 13, 8 (2005), 716–726.

Guanli Han, Baosheng Zhang, Yiyang Yu, Zhi Cheng, and Kuanli Yi. 2024. *Karman Vortex Street*. https://www.bilibili.com/video/BV1JUMue6EQK

Simone Elke Hieber and Petros Koumoutsakos. 2008. An immersed boundary method for smoothed particle hydrodynamics of self-propelled swimmers. *J. Comput. Phys.* 227, 19 (2008), 8636–8654.

David L Hu, Brian Chan, and John WM Bush. 2003. The hydrodynamics of water strider locomotion. *nature* 424, 6949 (2003), 663–666.

Yuanming Hu, Yu Fang, Ziheng Ge, Ziyin Qu, Yixin Zhu, Andre Pradhana, and Chenfanfu Jiang. 2018. A moving least squares material point method with displacement discontinuity and two-way rigid body coupling. *ACM Transactions on Graphics (TOG)* 37, 4 (2018), 1–14.

Yuanming Hu, Tzu-Mao Li, Luke Anderson, Jonathan Ragan-Kelley, and Frédo Durand. 2019. Taichi: a language for high-performance computation on spatially sparse data structures. *ACM Transactions on Graphics (TOG)* 38, 6 (2019), 201.

David AB Hyde and Ronald Fedkiw. 2019. A unified approach to monolithic solid-fluid coupling of sub-grid and more resolved solids. *J. Comput. Phys.* 390 (2019), 490–526.

Stefan Jeschke and Chris Wojtan. 2023. Generalizing shallow water simulations with dispersive surface waves. *ACM Transactions on Graphics (TOG)* 42, 4 (2023), 1–12.

Chenfanfu Jiang, Craig Schroeder, Andrew Selle, Joseph Teran, and Alexey Stomakhin. 2015. The affine particle-in-cell method. *ACM Transactions on Graphics (TOG)* 34, 4 (2015), 1–10.

Chenfanfu Jiang, Craig Schroeder, Joseph Teran, Alexey Stomakhin, and Andrew Selle. 2016. The material point method for simulating continuum materials. In *Acm siggraph 2016 courses*. 1–52.

Dustin Kleckner and William TM Irvine. 2013. Creation and dynamics of knotted vortices. *Nature physics* 9, 4 (2013), 253–258.
Nipun Kwatra, Jon Gretarsson, and Ronald Fedkiw. 2010. Practical Animation of Compressible Flow for ShockWaves and Related Phenomena.. In *Symposium on Computer Animation*. 207–215.
Nipun Kwatra, Jonathan Su, Jón T Grétarsson, and Ronald Fedkiw. 2009. A method for avoiding the acoustic time step restriction in compressible flow. *J. Comput. Phys.* 228, 11 (2009), 4146–4161.
Hyokwang Lee and Soonhung Han. 2010. Solving the shallow water equations using 2d sph particles for interactive applications. *The Visual Computer* 26 (2010), 865–872.
Zhiqi Li, Barnabás Börcsök, Duowen Chen, Yutong Sun, Bo Zhu, and Greg Turk. 2024a. Lagrangian Covector Fluid with Free Surface. In *ACM SIGGRAPH 2024 Conference Papers*. 1–10.
Zhiqi Li, Duowen Chen, Candong Lin, Jinyuan Liu, and Bo Zhu. 2024b. Particle-Laden Fluid on Flow Maps. *ACM Transactions on Graphics (TOG)* 43, 6 (2024), 1–12.
Xu-Dong Liu, Stanley Osher, and Tony Chan. 1994. Weighted essentially non-oscillatory schemes. *Journal of computational physics* 115, 1 (1994), 200–212.
Chaoyang Lyu, Kai Bai, Yiheng Wu, Mathieu Desbrun, Changxi Zheng, and Xiaopei Liu. 2023. Building a Virtual Weakly-Compressible Wind Tunnel Testing Facility. *ACM Transactions on Graphics (TOG)* 42, 4 (2023), 1–20.
Chaoyang Lyu, Wei Li, Mathieu Desbrun, and Xiaopei Liu. 2021. Fast and versatile fluid-solid coupling for turbulent flow simulation. *ACM Transactions on Graphics* 40, 6 (2021), 201.
D Mackenzie. 2006. Fluid Dynamics Explains Mysteries of Insect Motion. *WHATS HAPPENING IN THE MATHEMATICAL SCIENCES* 6 (2006), 86.
Joseph J Monaghan and Robert A Gingold. 1983. Shock simulation by the particle method SPH. *Journal of computational physics* 52, 2 (1983), 374–389.
Mohammad Sina Nabizadeh, Ritoban Roy-Chowdhury, Hang Yin, Ravi Ramamoorthi, and Albert Chern. 2024. Fluid Implicit Particles on Coadjoint Orbits. *arXiv preprint arXiv:2406.01936* (2024).
Mohammad Sina Nabizadeh, Stephanie Wang, Ravi Ramamoorthi, and Albert Chern. 2022. Covector fluids. *ACM Transactions on Graphics (TOG)* 41, 4 (2022), 1–16.
James F O'brien and Jessica K Hodgins. 1995. Dynamic simulation of splashing fluids. In *Proceedings Computer Animation'95*. IEEE, 198–205.
Zherong Pan, Jin Huang, Yiying Tong, and Hujun Bao. 2012. Wake synthesis for shallow water equation. In *Computer Graphics Forum*, Vol. 31. Wiley Online Library, 2029–2036.
Victor D Pareja. 2007. *Impulse formulations of the Euler equations for incompressible and compressible fluids*. University of Central Florida.
Ziyin Qu, Xinxin Zhang, Ming Gao, Chenfanfu Jiang, and Baoquan Chen. 2019. Efficient and conservative fluids using bidirectional mapping. *ACM Transactions on Graphics (TOG)* 38, 4 (2019), 1–12.
Wolfgang Rueckner. 2012. Vortex Shedding in Water. https://www.youtube.com/watch?v=_Hbbkd2d3H8 Harvard Natural Sciences Lecture Demonstrations..
Sergio Sancho, Jingwei Tang, Christopher Batty, and Vinicius C Azevedo. 2024. The Impulse Particle-In-Cell Method. In *Computer Graphics Forum*. Wiley Online Library, e15022.
Takahiro Sato, Christopher Batty, Takeo Igarashi, and Ryoichi Ando. 2018. Spatially adaptive long-term semi-Lagrangian method for accurate velocity advection. *Computational Visual Media* 4, 3 (2018), 6.
Takahiro Sato, Takeo Igarashi, Christopher Batty, and Ryoichi Ando. 2017. A long-term semi-lagrangian method for accurate velocity advection. In *SIGGRAPH Asia 2017 Technical Briefs*. 1–4.
Jason Sewall, Nico Galoppo, Georgi Tsankov, and Ming Lin. 2009. Visual simulation of shockwaves. *Graphical Models* 71, 4 (2009), 126–138.
Bhimsen K Shivamoggi. 2010. Hydrodynamic impulse in a compressible fluid. *Physics Letters A* 374, 47 (2010), 4736–4740.
Chi-Wang Shu and Stanley Osher. 1988. Efficient implementation of essentially non-oscillatory shock-capturing schemes. *Journal of computational physics* 77, 2 (1988), 439–471.
William Snow. 1967. Survey of acoustic characteristics of bullet shock waves. *IEEE Transactions on Audio and Electroacoustics* 15, 4 (1967), 161–176.
Barbara Solenthaler, Peter Bucher, Nuttapong Chentanez, Matthias Müller, and Markus Gross. 2011. SPH based shallow water simulation. (2011).
Jos Stam and Eugene Fiume. 1995. Depicting fire and other gaseous phenomena using diffusion processes. In *Proceedings of the 22nd annual conference on Computer graphics and interactive techniques*. 129–136.
Yuchen Sun, Linglai Chen, Weiyuan Zeng, Tao Du, Shiying Xiong, and Bo Zhu. 2024. An Impulse Ghost Fluid Method for Simulating Two-Phase Flows. *ACM Transactions on Graphics (TOG)* 43, 6 (2024), 1–12.
Jerry Tessendorf. 2015. Advection Solver Performance with Long Time Steps, and Strategies for Fast and Accurate Numerical Implementation. (2015).
Huamin Wang, Gavin Miller, and Greg Turk. 2007. Solving general shallow wave equations on surfaces. In *Proceedings of the 2007 ACM SIGGRAPH/Eurographics symposium on Computer animation*. 229–238.
Sinan Wang, Yitong Deng, Molin Deng, Hong-Xing Yu, Junwei Zhou, Duowen Chen, Taku Komura, Jiajun Wu, and Bo Zhu. 2024. An Eulerian Vortex Method on Flow Maps. *ACM Transactions on Graphics (TOG)* 43, 6 (2024), 1–14.
DC Wiggert and EB Wylie. 1976. Numerical predictions of two-dimensional transient groundwater flow by the method of characteristics. *Water Resources Research* 12, 5 (1976), 971–977.
Jie-Zhi Wu, Hui-Yang Ma, and M-D Zhou. 2007. *Vorticity and vortex dynamics*. Springer Science & Business Media.
Xi-Yuan Yin, Olivier Mercier, Badal Yadav, Kai Schneider, and Jean-Christophe Nave. 2021. A characteristic mapping method for the two-dimensional incompressible Euler equations. *J. Comput. Phys.* 424 (2021), 109781.
Xi-Yuan Yin, Kai Schneider, and Jean-Christophe Nave. 2023. A Characteristic Mapping Method for the three-dimensional incompressible Euler equations. *J. Comput. Phys.* 477 (2023), 111876.
Gary D Yngve, James F O'Brien, and Jessica K Hodgins. 2000. Animating explosions. In *Proceedings of the 27th annual conference on Computer graphics and interactive techniques*. 29–36.
Junwei Zhou, Duowen Chen, Molin Deng, Yitong Deng, Yuchen Sun, Sinan Wang, Shiying Xiong, and Bo Zhu. 2024. Eulerian-Lagrangian Fluid Simulation on Particle Flow Maps. *ACM Transactions on Graphics (TOG)* 43, 4 (2024), 1–20.
Bo Zhu, Xubo Yang, and Ye Fan. 2010. Creating and preserving vortical details in sph fluid. In *Computer Graphics Forum*, Vol. 29. Wiley Online Library, 2207–2214.

A Proof of Eq. 8

For generality, we leave $\mathbf{f} = 0$. Substituting $\mathbf{m} = \mathbf{u} + \frac{1}{\rho}\nabla\tilde{\Lambda}$ into the first line of Equation 6, we get:

$$\begin{aligned}
&\frac{D}{Dt}(\mathbf{m} - \frac{1}{\rho}\nabla\tilde{\Lambda}) = -\frac{1}{\rho}\nabla p + \mathbf{f}\\
&\frac{D}{Dt}\mathbf{m} = \frac{1}{\rho}\frac{D\nabla\tilde{\Lambda}}{Dt} + \frac{D\frac{1}{\rho}}{Dt}\nabla\tilde{\Lambda} - \frac{1}{\rho}\nabla p + \mathbf{f} \overset{①}{\Rightarrow}\\
&\frac{D}{Dt}\mathbf{m} = \frac{1}{\rho}(\nabla\frac{D\tilde{\Lambda}}{Dt} - \nabla\mathbf{u}^\top\nabla\tilde{\Lambda}) - \frac{1}{\rho^2}\frac{D\rho}{Dt}\nabla\tilde{\Lambda} - \frac{1}{\rho}\nabla p + \mathbf{f}
\end{aligned} \tag{32}$$

where ① holds because for any scalar field q, the equation holds

$$\frac{D\nabla q}{Dt} = \nabla\frac{Dq}{Dt} - \nabla\mathbf{u}^\top\nabla q \tag{33}$$

Rearranging the above equation with the equations $\mathbf{m}_t = \mathbf{u}_t + \frac{1}{\rho}\nabla\tilde{\Lambda}_t$ and $\frac{D\rho}{Dt} + (\nabla\cdot\mathbf{u})\rho = 0$, we get:

$$\begin{aligned}
&\frac{D}{Dt}\mathbf{m} + \nabla\mathbf{u}^\top\mathbf{m} - (\nabla\cdot\mathbf{u})\mathbf{m}\\
&\qquad = \frac{1}{\rho}\nabla(\frac{D\tilde{\Lambda}}{Dt} - p + \frac{1}{2}\rho|\mathbf{u}|^2) - (\nabla\cdot\mathbf{u})\mathbf{u} - \frac{\nabla\rho}{2\rho}|\mathbf{u}|^2 + \mathbf{f}
\end{aligned} \tag{34}$$

Let $\frac{D\tilde{\Lambda}}{Dt} - p + \frac{1}{2}\rho|\mathbf{u}|^2 = 0$ for $\tilde{\Lambda}$ in gauge transformation, similar to [Cortez 1996], we have:

$$\frac{D}{Dt}\mathbf{m} + \nabla\mathbf{u}^\top\mathbf{m} - (\nabla\cdot\mathbf{u})\mathbf{m} = -(\nabla\cdot\mathbf{u})\mathbf{u} - \frac{\nabla\rho}{2\rho}|\mathbf{u}|^2 + \mathbf{f} \tag{35}$$

The above equation has a solution:

$$\begin{aligned}
&\mathbf{m}_t(\mathbf{x}) = \frac{\mathcal{T}_{t\to s}^\top(\mathbf{x})}{|\mathcal{T}_{t\to s}(\mathbf{x})|}\mathbf{u}_s(\mathbf{\Psi}_{t\to s}(\mathbf{x})) + \frac{\mathcal{T}_{t\to s}^\top(\mathbf{x})}{|\mathcal{T}_{t\to s}(\mathbf{x})|}\mathcal{E}_{s\to t}(\mathbf{\Psi}_{t\to s}(\mathbf{x}))\\
&\mathcal{E}_{s\to t}(\mathbf{x}) = \int \frac{\mathcal{F}_{s\to\tau}^\top(\mathbf{x})}{|\mathcal{F}_{s\to\tau}(\mathbf{x})|}(-\frac{\nabla\rho}{2\rho}\nabla|\mathbf{u}_\tau|^2 - (\nabla\cdot\mathbf{u}_\tau)\mathbf{u}_\tau + \mathbf{f})(\mathbf{\Phi}_{s\to\tau}(\mathbf{x}))d\tau
\end{aligned} \tag{36}$$

which can be easily verified by substituting *Equation* 36 into *Equation* 35.

B Proof of Eq. 10

First, we substitute the expression of $m_t(\mathbf{x})$ from Equation 10 into the equation $\mathbf{u}_t(\mathbf{x}) = \mathbf{m}_t(\mathbf{x}) - \frac{1}{\rho_t}\nabla\tilde{\Lambda}_t(\mathbf{x})$ to obtain the formula for computing $\mathbf{u}_t(\mathbf{x})$:

$$\begin{aligned}&\mathbf{u}_t(\mathbf{x}) = \frac{\mathcal{T}^\top_{t\to s}(\mathbf{x})}{|\mathcal{T}_{t\to s}(\mathbf{x})|}\mathbf{u}_s(\mathbf{\Psi}_{t\to s}(\mathbf{x}))+\\ &\frac{\mathcal{T}^\top_{t\to s}(\mathbf{x})}{|\mathcal{T}_{t\to s}(\mathbf{x})|}\int\frac{\mathcal{F}^\top_{s\to\tau}(\mathbf{x})}{|\mathcal{F}_{s\to\tau}(\mathbf{x})|}(-\frac{\nabla\rho}{2\rho}|\mathbf{u}_\tau|^2-(\nabla\cdot\mathbf{u}_\tau)\mathbf{u}_\tau+\mathbf{f})_\tau(\mathbf{\Psi}_{t\to\tau}(\mathbf{x}))d\tau\\ &-\frac{1}{\rho_t}\nabla\int_s^t(p-\frac{1}{2}\rho|\mathbf{u}|^2)_\tau(\mathbf{\Psi}_{t\to\tau}(\mathbf{x}))d\tau\end{aligned} \tag{37}$$

where $\mathbf{\Psi}_{t\to\tau}$ is short for $\mathbf{\Phi}_{s\to\tau}\circ\mathbf{\Psi}_{t\to s}$.

The above expression contains two integral terms and now we aim to merge them. First, it can be shown that the vector fields $\mathbf{\Theta}_2(\mathbf{x},t) = \frac{\mathcal{T}^\top_{t\to s}(\mathbf{x})}{|\mathcal{T}_{t\to s}(\mathbf{x})|}\int_s^t\frac{\mathcal{F}^\top_{s\to\tau}(\mathbf{x})}{|\mathcal{F}_{s\to\tau}(\mathbf{x})|}(\frac{1}{\rho_\tau}\nabla q_\tau)(\mathbf{\Phi}_{s\to\tau}\circ\mathbf{\Psi}_{t\to s}(\mathbf{x}))d\tau$ and $\mathbf{\Theta}_1(\mathbf{x},t) = \frac{1}{\rho_t(\mathbf{x})}\nabla\int_s^t q_\tau(\mathbf{\Phi}_{s\to\tau}\circ\mathbf{\Psi}_{t\to s}(\mathbf{x}))d\tau$ are equal for any scalar field q_t, because $\mathbf{\Theta}_1(\mathbf{x},s) = \mathbf{\Theta}_2(\mathbf{x},s) = 0$ and they satisfy the same evolution equation, which we prove as follows.

For $\mathbf{\Theta}_1(\mathbf{x},t)$, applying $\frac{D}{Dt}$ to both sides of the equation $\rho_t(\mathbf{x})\mathbf{\Theta}_1(\mathbf{x},t) = \nabla\int_s^t q_\tau(\mathbf{\Phi}_{s\to\tau}\circ\mathbf{\Psi}_{t\to s}(\mathbf{x}))d\tau$, we obtain:

$$\begin{aligned}&\frac{D(\rho_t(\mathbf{x})\mathbf{\Theta}_1(\mathbf{x},t))}{Dt} = \frac{D}{Dt}\nabla\int_s^t q_\tau(\mathbf{\Phi}_{s\to\tau}\circ\mathbf{\Psi}_{t\to s}(\mathbf{x}))d\tau \overset{②}{\Rightarrow}\\ &\rho_t(\mathbf{x})\frac{D\mathbf{\Theta}_1(\mathbf{x},t)}{Dt}+\frac{D\rho_t(\mathbf{x})}{Dt}\mathbf{\Theta}_1(\mathbf{x},t) = \nabla q_t(\mathbf{x})-\nabla u^\top\rho_t(\mathbf{x})\mathbf{\Theta}_1(\mathbf{x},t)\overset{③}{\Rightarrow}\\ &\rho_t(\mathbf{x})\frac{D\mathbf{\Theta}_1(\mathbf{x},t)}{Dt}-\rho_t(\mathbf{x})(\nabla\cdot u)\mathbf{\Theta}_1(\mathbf{x},t) = \nabla q(\mathbf{x})-\nabla u^\top\rho_t(\mathbf{x})\mathbf{\Theta}_1(\mathbf{x},t)\end{aligned} \tag{38}$$

where ② holds due to Equation 33 and ③ holds due to ρ_t satisfy $\frac{D\rho}{Dt}+(\nabla\cdot\mathbf{u})\rho = 0$

For $\mathbf{\Theta}_2(\mathbf{x},t)$, applying $\frac{D}{Dt}$ to both sides of the following equation $\mathcal{T}^{-T}_{t\to s}(\mathbf{x})|\mathcal{T}_{t\to s}(\mathbf{x})|\mathbf{\Theta}_2(\mathbf{x},t) = \int_s^t\frac{\mathcal{F}^\top_{s\to\tau}}{|\mathcal{F}_{s\to\tau}|}(\frac{1}{\rho_\tau}\nabla q_\tau)(\mathbf{\Phi}_{s\to\tau}\circ\mathbf{\Psi}_{t\to s}(\mathbf{x}))d\tau$, based on the evolution equation of $\mathcal{T}_{t\to s}(x)$, we obtain:

$$\begin{aligned}&\frac{D(\mathcal{T}^{-T}_{t\to s}(\mathbf{x})|\mathcal{T}_{t\to s}(\mathbf{x})|\mathbf{\Theta}_2(\mathbf{x},t))}{Dt} = \frac{\mathcal{F}^\top_{s\to t}}{|\mathcal{F}_{s\to t}|}\frac{1}{\rho_t}\nabla q_t(\mathbf{x})\Rightarrow\\ &\mathcal{T}^{-\top}_{t\to s}(x)\nabla u^\top|\mathcal{T}_{t\to s}(\mathbf{x})|\mathbf{\Theta}_2(\mathbf{x},t)+\mathcal{T}^{-T}_{t\to s}(\mathbf{x})(-\nabla\cdot u)|\mathcal{T}_{t\to s}(\mathbf{x})|\mathbf{\Theta}_2(\mathbf{x},t))\\ &+\mathcal{T}^{-T}_{t\to s}(\mathbf{x})|\mathcal{T}_{t\to s}(\mathbf{x})|\frac{D\mathbf{\Theta}_2(\mathbf{x},t)}{Dt} = \frac{\mathcal{F}^\top_{s\to t}}{|\mathcal{F}_{s\to t}|}(\frac{1}{\rho_t}\nabla q_t)(\mathbf{x})\end{aligned} \tag{39}$$

After organizing, it was found that $\mathbf{\Theta}_1$ and $\mathbf{\Theta}_2$ both satisfy the evolution equation: $\frac{D\mathbf{\Theta}}{Dt} = (\nabla\cdot\mathbf{u})\mathbf{\Theta}+\frac{1}{\rho}\nabla q-(\nabla u)^\top\mathbf{\Theta}$

Therefore, the two integral terms in Equation 37 can be unified after transforming the second integral using the equivalence of $\mathbf{\Theta}_1$ and $\mathbf{\Theta}_2$, leading to:

$$\begin{aligned}&\mathbf{u}_t(\mathbf{x}) = \frac{\mathcal{T}^\top_{t\to s}(\mathbf{x})}{|\mathcal{T}_{t\to s}(\mathbf{x})|}\mathbf{u}_s(\mathbf{\Psi}_{t\to s}(\mathbf{x}))+\\ &\frac{\mathcal{T}^\top_{t\to s}(\mathbf{x})}{|\mathcal{T}_{t\to s}(\mathbf{x})|}\int\frac{\mathcal{F}^\top_{s\to\tau}(\mathbf{x})}{|\mathcal{F}_{s\to\tau}(\mathbf{x})|}(-\frac{\nabla\rho}{2\rho}|\mathbf{u}_\tau|^2-(\nabla\cdot\mathbf{u}_\tau)\mathbf{u}_\tau+\mathbf{f})_\tau(\mathbf{\Psi}_{t\to\tau}(\mathbf{x}))d\tau\\ &-\frac{\mathcal{T}^\top_{t\to s}(\mathbf{x})}{|\mathcal{T}_{t\to s}(\mathbf{x})|}\int\frac{\mathcal{F}^\top_{s\to\tau}(\mathbf{x})}{|\mathcal{F}_{s\to\tau}(\mathbf{x})|}(\frac{1}{\rho}\nabla(p-\frac{1}{2}\rho|\mathbf{u}|^2)_\tau(\mathbf{\Psi}_{t\to\tau}(\mathbf{x}))d\tau\end{aligned} \tag{40}$$

which proves Equation 10 with $\frac{1}{\rho}\nabla(\frac{1}{2}\rho|\mathbf{u}|^2)-\frac{\nabla\rho}{2\rho}\nabla|\mathbf{u}|^2 = \frac{1}{2}\nabla|\mathbf{u}|^2$ holds.

C Proof of Equivalence between Eq. 10 & 12

To prove that Equation 10 is equivalent to Equation 12 in all cases, we distinguish between them as follows: regardless of the incompressibility condition, let $\mathbf{u}^I$ and $\mathbf{u}^C$ denote the velocities computed by Equation 12 and Equation 10, respectively, and let $\tilde{\mathcal{E}}^I$ and $\tilde{\mathcal{E}}^C$ represent the corresponding $\tilde{\mathcal{E}}$ terms of $\mathbf{u}^I$ and $\mathbf{u}^C$. Since $\mathbf{u}^C_s(\mathbf{x}) = \mathbf{u}^I_s(\mathbf{x})$, it suffices to prove that $\mathbf{u}^I$ and $\mathbf{u}^C$ satisfy the same evolution equation in all cases.

For $\mathbf{u}^C$, applying $\frac{D}{Dt}$ to both sides of $\mathcal{T}^{-\top}_{t\to s}(\mathbf{x})|\mathcal{T}_{t\to s}(\mathbf{x})|\mathbf{u}^C_t(\mathbf{x}) = \mathbf{u}_s(\mathbf{\Psi}_{t\to s}(\mathbf{x}))+\tilde{\mathcal{E}}^C_{s\to t}(\mathbf{\Psi}_{t\to s}(\mathbf{x}))$, we obtain:

$$\begin{aligned}&\frac{D(\mathcal{T}^{-\top}_{t\to s}(\mathbf{x})|\mathcal{T}_{t\to s}(\mathbf{x})|\mathbf{u}^C_t(\mathbf{x}))}{Dt}\\ &= \frac{\mathcal{F}^\top_{s\to\tau}(\mathbf{x})}{|\mathcal{F}_{s\to\tau}(\mathbf{x})|}(-\frac{1}{\rho}\nabla p+\frac{1}{2}\nabla|\mathbf{u}^C|^2-(\nabla\cdot\mathbf{u}^C)\mathbf{u}^C+\mathbf{f})(\mathbf{x},t)\Rightarrow\\ &\mathcal{T}^{-\top}_{t\to s}(\mathbf{x})\nabla\mathbf{u}^\top|\mathcal{T}_{t\to s}(\mathbf{x})|\mathbf{u}^C_t(\mathbf{x})+\mathcal{T}^{-T}_{t\to s}(\mathbf{x})(-\nabla\cdot\mathbf{u})|\mathcal{T}_{t\to s}(\mathbf{x})|\mathbf{u}^C_t(\mathbf{x})\\ &+\mathcal{T}^{-T}_{t\to s}(\mathbf{x})|\mathcal{T}_{t\to s}(\mathbf{x})|\frac{D\mathbf{u}^C_t(\mathbf{x})}{Dt}\\ &= \frac{\mathcal{F}^\top_{s\to t}(\mathbf{x})}{|\mathcal{F}_{s\to t}(\mathbf{x})|}(-\frac{1}{\rho}\nabla p+\frac{1}{2}\nabla|\mathbf{u}^C|^2-(\nabla\cdot\mathbf{u}^C)\mathbf{u}^C+\mathbf{f})(\mathbf{x},t)\end{aligned} \tag{41}$$

The calculation above is similar to the calculation for $\Theta_2(x,t)$ in Appendix B.

For u^I, applying $\frac{D}{Dt}$ to both sides of $\mathcal{T}^{-\top}_{t\to s}(\mathbf{x})\mathbf{u}^I_t(\mathbf{x}) = \mathbf{u}_s(\mathbf{\Psi}_{t\to s}(\mathbf{x}))+\tilde{\mathcal{E}}^I_{s\to t}(\mathbf{\Psi}_{t\to s}(\mathbf{x}))$, we obtain:

$$\begin{aligned}&\frac{D(\mathcal{T}^{-\top}_{t\to s}(\mathbf{x})\mathbf{u}^I_t(\mathbf{x}))}{Dt} = \mathcal{F}^\top_{s\to\tau}(\mathbf{x})(-\frac{1}{\rho}\nabla p+\frac{1}{2}\nabla|\mathbf{u}|^2+\mathbf{f})(x,t)\Rightarrow\\ &\mathcal{T}^{-\top}_{t\to s}(\mathbf{x})\nabla\mathbf{u}^\top\mathbf{u}^I_t(\mathbf{x})+\mathcal{T}^{-T}_{t\to s}(\mathbf{x})\frac{D\mathbf{u}^I_t(\mathbf{x})}{Dt}\\ &= \mathcal{F}^\top_{s\to t}(\mathbf{x})(-\frac{1}{\rho}\nabla p+\frac{1}{2}\nabla|\mathbf{u}^I|^2+\mathbf{f})(\mathbf{x},t)\end{aligned} \tag{42}$$

After organizing, it was found that $\mathbf{u}^I$ and $\mathbf{u}^C$ both satisfy the evolution equation:

$$\frac{D\mathbf{u}}{Dt} = -\frac{1}{\rho}\nabla p+\mathbf{f} \tag{43}$$

D Derivation of Eq. 12 & 13 by 1-form Notation

Similar to [Nabizadeh et al. 2022], we reformulated Equation 6 as $\frac{\partial\mathbf{u}}{\partial t}+(\mathbf{u}\cdot\nabla)\mathbf{u}+\nabla\mathbf{u}^T\cdot\mathbf{u} = \mathbf{f}-\frac{1}{\rho}\nabla p+\frac{1}{2}|\mathbf{u}|^2$ and expressed it in

1-form using the Lie derivative

$$\left(\frac{\partial}{\partial t}+L_{\mathbf{u}}\right)\mathbf{u}^\flat=\mathbf{f}^\flat-\frac{1}{\rho}dp+\frac{1}{2}d|\mathbf{u}|^2 \tag{44}$$

This equality holds because, in $\mathbb{R}^d$, $(L_{\mathbf{u}}\mathbf{v}^\flat)^\sharp=(\mathbf{u}\cdot\nabla)\mathbf{v}+(\nabla\mathbf{u})^\top\mathbf{v}$ holds for any vector field $\mathbf{v}$.

By integrating this equation of Lie derivative form, we obtain

$$\begin{aligned}\mathbf{u}_r^\flat&=\Psi_{r\to s}^*\mathbf{u}_s^\flat+\int_s^t(\Phi_{s\to\tau}\circ\Psi_{r\to s})^*(\mathbf{f}^\flat-\frac{1}{\rho}dp+\frac{1}{2}d|\mathbf{u}|^2)d\tau\\&=\Psi_{r\to s}^*\mathbf{u}_s^\flat+\Psi_{r\to s}^*\int_s^t\Phi_{s\to\tau}^*(\mathbf{f}^\flat-\frac{1}{\rho}dp+\frac{1}{2}d|\mathbf{u}|^2)d\tau\end{aligned} \tag{45}$$

where $\Psi_{r\to s}^*$ and $\Phi_{s\to\tau}^*$ are the pullbacks of 1-form induced by $\Psi_{r\to s}$ and $\Phi_{s\to\tau}$, respectively (see [Crane et al. 2013] for detials of pullback and 1-form). Convert the above expression back to vector form, and noting that $\Psi_{r\to s}^*\mathbf{v}^\flat$ and $\Phi_{s\to\tau}^*\mathbf{v}^\flat$ corresponds to $\nabla\Psi_{r\to s}^\top\mathbf{v}$ and $\nabla\Phi_{s\to\tau}^\top\mathbf{v}$ respectively for arbitrary vector field $\mathbf{v}$, we then get Equation 12.

To prove Equation 13, we first define $V_t(\mathbf{x})=|\mathcal{F}_{s\to t}(\Psi_{t\to s}(\mathbf{x}))|$, which represents the volume change induced by the forward mapping. V_t satisfies the evolution equation $\frac{DV}{Dt}=V\nabla\cdot\mathbf{u}$. Then, we begin by reformulating Equation 6 into an equation for $\frac{\mathbf{u}}{V}$, yielding:

$$(\frac{\partial}{\partial t}+\mathbf{u}\cdot\nabla)\frac{\mathbf{u}}{V}+(\nabla\mathbf{u})^\top\frac{\mathbf{u}}{V}=\frac{1}{V}(f-\frac{1}{\rho}\nabla p+\frac{1}{2}|\mathbf{u}|^2-(\nabla\cdot\mathbf{u})\mathbf{u}) \tag{46}$$

Expressing the above equation in the form of a 1-form, we obtain: $\left(\frac{\partial}{\partial t}+L_{\mathbf{u}}\right)\frac{\mathbf{u}^\flat}{V}=\frac{1}{V}(\mathbf{f}^\flat-\frac{1}{\rho}dp+\frac{1}{2}d|\mathbf{u}|^2-(\nabla\cdot\mathbf{u})\mathbf{u}^\flat)$ By integrating this equation of Lie derivative form, we obtain

$$\begin{aligned}(\frac{\mathbf{u}^\flat}{|V|})_r&=\Psi_{r\to s}^*\mathbf{u}_s^\flat\\&\quad+\int_s^t(\Phi_{s\to\tau}\circ\Psi_{r\to s})^*\frac{1}{V}(\mathbf{f}^\flat-\frac{1}{\rho}dp+\frac{1}{2}d|\mathbf{u}|^2-(\nabla\cdot\mathbf{u})\mathbf{u}^\flat)d\tau\\&=\Psi_{r\to s}^*\mathbf{u}_s^\flat\\&\quad+\Psi_{r\to s}^*\int_s^t\Phi_{s\to\tau}^*\frac{1}{V}(\mathbf{f}^\flat-\frac{1}{\rho}dp+\frac{1}{2}d|\mathbf{u}|^2-(\nabla\cdot\mathbf{u})\mathbf{u}^\flat)d\tau\end{aligned} \tag{47}$$

Convert the above expression back to vector form, and noting that $V_t(\mathbf{x})=|\mathcal{F}_{s\to t}(\Psi_{t\to s}(\mathbf{x}))|=\frac{1}{|\mathcal{T}_{t\to s}(\mathbf{x})|}$ we then get Equation 13.

E Proof of Eq. 16

To validate Equation 16 is the solution of Equation 15, it suffices to verify the following:

$$\begin{aligned}\frac{Dq(\mathbf{x},t)}{Dt}&=\frac{D(|\mathcal{T}_{s\to t}(\mathbf{x})|^\theta q_s(\mathbf{\Psi}(\mathbf{x},t)))}{Dt}\\&=|\mathcal{T}_{s\to t}(\mathbf{x})|^\theta\frac{Dq_s(\mathbf{\Psi}(\mathbf{x},t))}{Dt}+\frac{D|\mathcal{T}_{s\to t}(\mathbf{x})|^\theta}{Dt}q_s(\mathbf{\Psi}(\mathbf{x},t))\overset{⑤}{\Rightarrow}\\&=\theta|\mathcal{T}_{s\to t}(\mathbf{x})|^{\theta-1}(-|\mathcal{T}_{s\to t}(\mathbf{x})|(\nabla\cdot\mathbf{u}))q_s(\mathbf{\Psi}(\mathbf{x},t))\\&=-\theta(\nabla\cdot\mathbf{u})q(\mathbf{x},t)\end{aligned} \tag{48}$$

where ⑤ holds because $\frac{Dq_s(\mathbf{\Psi}(\mathbf{x},t))}{Dt}=0$ and $|\mathcal{T}_{s\to t}|$ satisfy advection equation $\frac{D|\mathcal{T}_{s\to t}|}{Dt}=-|\mathcal{T}_{s\to t}|(\nabla\cdot\mathbf{u})$